Accepted Manuscript

A novel chitosan-based nanomedicine for multi-drug resistant breast cancer therapy

Shiwei Niu, Gareth R. Williams, Jianrong Wu, Junzi Wu, Xuejing Zhang, Hong Zheng, Shude Li, Li-Min Zhu

Please cite this article as: S. Niu, G.R. Williams, J. Wu, J. Wu, X. Zhang, H. Zheng, S. Li, L-M. Zhu, A novel chitosan-based nanomedicine for multi-drug resistant breast cancer therapy, *Chemical Engineering Journal* (2019), doi: https://doi.org/10.1016/j.cej.2019.02.201

A novel chitosan-based nanomedicine for multi-drug resistant breast cancer therapy

Shiwei Niu[1], Gareth R. Williams[2], Jianrong Wu[1], Junzi Wu[3], Xuejing Zhang[1], Hong Zheng[4], Shude Li[5*], Li-Min, Zhu[1*]

[1]College of Chemistry, Chemical Engineering and Biotechnology, Donghua University, Shanghai, PR China

[2]UCL School of Pharmacy, University College London, 29-39 Brunswick Square, London, WC1N 1AX, UK

[3]School of Basic Medicine, Yunnan University of Traditional Chinese Medicine, Kunming 650500, PR China

[4]Department of Laboratory Animal Science, Kunming Medical University, Kunming 650500, PR China

[5]Department of Biochemistry and Molecular Biology, School of Basic Medicine, Kunming Medical University, Kunming 650500, PR China

Authors for correspondence:

Li-Min Zhu, College of Chemistry, Chemical Engineering and Biotechnology, Donghua University, Shanghai 201620, PR China. Tel: +86 13564410208. Email: lzhu@dhu.edu.cn

Shude Li, Department of Biochemistry and Molecular Biology, School of Basic Medicine, Kunming Medical University, Kunming 650500, PR China Tel: +86 13529227380. Email: shudeli006@vip.sina.com

ABSTRACT

In this study, a novel chitosan-based (CS) nanocarrier was developed for doxorubicin (DOX) and oleanolic acid (OA) co-delivery. CS was first functionalized with folic acid to allow selective uptake by cancer cells, and then subsequently with OA. The resultant copolymer self-assembled into nanoparticles (NPs) upon addition to water. These FA-CS-g-OA@DOX nanoparticles (NPs) had appropriate size (180 nm) and size distribution (PDI < 0.45) for tumor therapy, as well as a high drug-loading efficiency (15.6 % w/w DOX; 5.1% w/w OA) and pH-responsive release properties. In breast cancer MDA-MB-231 cells, more efficient uptake of FA-CS-g-OA@DOX NPs than of free DOX was observed by confocal laser scanning microscopy and flow cytometry. The *in vitro* cytotoxicity of FA-CS-g-OA@DOX NPs against MDA-MB-231 cells was higher than with free DOX and free OA, while the NPs were less harmful to healthy HUVEC cells. *In vivo* pharmacokinetic studies showed that FA-CS-g-OA@DOX NPs had a much longer circulation time than free DOX, while biodistribution results revealed that FA-CS-g-OA@DOX could actively target a MDA-MB-231 xenograft tumor in mice. The NPs are found to have apoptosis-enhancing and anti-proliferative capacities *in vivo*. The presence of OA in the formulation both sensitizes cancer cells to DOX and mitigates DOX-induced damage to healthy tissues. The FA-CS-g-OA@DOX NPs generated in this work hence have great potential for the treatment of multi-drug resistant breast cancers, and further offer a platform to target other cancers.

Keywords: Chitosan-based nanocarrier; Doxorubicin; Oleanolic acid; Codelivery; Chemosensitizing

1. Introduction

Cancer remains one of the leading cause of death worldwide, and the estimated number of patients who will suffer from cancer in the future is enormous. In 2012, more than 14 million new cases were reported, and 8.2 million patients died of cancer [1]. Although tremendous progress has been made in cancer therapy over recent decades, there remain many cases where patients cannot be cured. This is particularly true for breast cancer, which is the most prevalent cancer in women: only 23% of stage IV breast cancer subjects survive beyond five years [2]. Various therapeutic interventions have been applied clinically to treat tumors in the breast, including chemotherapy, photothermal therapy, radiotherapy, photodynamic therapy, and immunotherapy [3].

Chemotherapy is the predominant approach employed, and relies on the high cytotoxicity of the active ingredients delivered (e. g. doxorubicin, paclitaxel, gemcitabine, 5-fluorouracil). However, these agents are non-specific and cause damage to normal as well as cancerous tissues. They also often have poor aqueous solubility, low bioavailability, and rapid blood clearance times; in addition, there exist therapy-resistant cancer cells which cannot effectively be treated with chemotherapeutic active ingredients [4-6]. In order to address these difficulties, the use of nanoscale carriers for chemotherapeutics has been widely explored. Such carriers can improve the solubility and targeting efficiency of anti-tumor drugs [7], as well as protecting them from rapid blood/renal clearance. They can also facilitate the preferential accumulation of drugs within solid tumors due to the enhanced permeability and retention (EPR) effect [8]. In recent decades, a wide range of novel drug delivery systems (DDSs) such as liposomes, hydrogels, micelles and polymer nanoparticles (NPs) have been designed as vehicles to improve efficacy and reduce side effects. Among these, polymer NPs in particular have shown potential clinical applications in the treatment of cancer. Numerous studies have confirmed that NPs can control the drug release rate to prolong treatment times and enhance the accumulation of the active ingredient at the lesion site *in vivo* [9-11].

To develop NP-based anti-cancer formulations, a number of design parameters must be considered. The polymers selected should be biocompatible, biodegradable, and have low toxicity. Chitosan (CS) is one material which has been widely recognized as suitable for the construction of such NPs: it is a natural cationic carbohydrate, with good biocompatibility, low immunogenicity, and the potential to facilitate transport across cell membranes [12]. Importantly, under the action of enzymes *in vivo*, CS is degraded to the endogenous species water and carbon dioxide [13]. CS can also be used for pH-responsive drug delivery by virtue of its elevated solubility in slightly acidic environments (such as the tumor microenvironment) [14]. In order to enhance specific recognition of a DDS by tumor tissues (so-called "active targeting"), nanocarriers usually require further modification with tumor–homing ligands, such as peptides, antibodies, nucleic acids or small molecules [15]. For instance, folic acid (FA) receptors are overexpressed on tumor cells. Hence, grafting FA to NPs can endow them with an active targeting capacity. CS NPs in general have high biocompatibility, but it is often desirable to add additional surface modifications to e.g. increase circulation times and inhibit an immune response. However, this typically introduces

extraneous materials (e.g. *N*-isopropylacrylamide, poly (ethylene glycol), gold nanoparticles, mesoporous silica) which can lead to systemic toxicity in healthy tissues. To overcome this issue, a strategy based on the selection of biocompatible copolymers containing hydrophobic segments to provide a lipophilic core for drug storage has been proposed [16].

Oleanolic acid (OA) is a naturally occurring pentacyclic triterpenoid which can be isolated from a range of plant species, particularly those belonging to the Oleaceae family. It possesses many interesting biological activities, for example being reported to have antioxidant, anti-inflammatory, and anti-fibrosis effects [17]. Previous studies have found that OA could improve renal function and protect hepatocytes against oxidative stress *in vitro*, with an OA treatment exerting anti-inflammatory effects through down-regulating pro-inflammatory factors (e.g. IL-6, IL-1β, TNF-α) [15, 18]. In addition, OA is able to affect different stages of tumorigenesis, suppressing tumor initiation and promotion, and inducing cell apoptosis [19-21].

Tumor cell invasion through the stroma is influenced by signals from the microenvironment, including the extracellular matrix (ECM), cytokines, and stromal cells [22]. In several types of cancer, the fibrotic stroma provides a physical barrier to inhibit the distribution and penetration of antitumor drugs [5]. However, the activities of matrix metalloproteinases (MMPs) can be eliminated by OA, suggesting it has potential for ameliorating the fibrosis of tumor stromal cells [23]. All these findings indicate that OA could act as a potent adjunct to cancer chemotherapy [24].

Multidrug resistance (MDR) is the main cause of failure in the chemotherapy of cancer patients [25]. MDR is mainly related to the overexpression of membrane transporter proteins (P-glycoprotein (P-gp) and the multidrug resistance protein (MRP)), which act to expel anticancer drugs from cancer cells [26]. This profoundly decreases the sensitivity of the tumor to chemotherapy. The action of OA against multidrug resistant tumor cells overexpressing MDR-associated factors has been examined [27], and it was found that OA could enhance the cytotoxic effects of anticancer agents owing to inhibition of MRP and P-gp, and the consequent reversal of MRP-mediated efflux. This allows OA to impart a chemosensitizing effect [28].

In this study, we functionalized CS with FA to generate FA-CS NPs with active targeting properties. Subsequently, OA was conjugated to the CS backbone (yielding FA-CS-g-OA) to prolong blood circulation and enhance therapeutic efficacy. In addition, the introduction of

hydrophobic OA will result in an amphiphilic polymer system which can self-assemble to form spheres with a core-shell structure upon addition to water. These will have a hydrophobic core into which low-solubility drugs such as doxorubicin (DOX) can be loaded. This approach is illustrated in Scheme 1. By bringing together CS, FA, OA and DOX into a simple nanoformulation, we prepare a novel system which can simultaneously i) be taken up selectively by breast cancer cells; ii) give accelerated drug release at the slightly acidic pH of the tumor microenvironment; iii) prevent the occurrence of MDR; and iv) provide highly effective treatment of tumors while ameliorating the off-target side effects common with chemotherapy. The materials developed in our work offer a new chemical engineering approach to prepare multifunctional nanoparticles. The platform approach reported here for the first time has broad applicability in the treatment of a range of diseases and conditions.
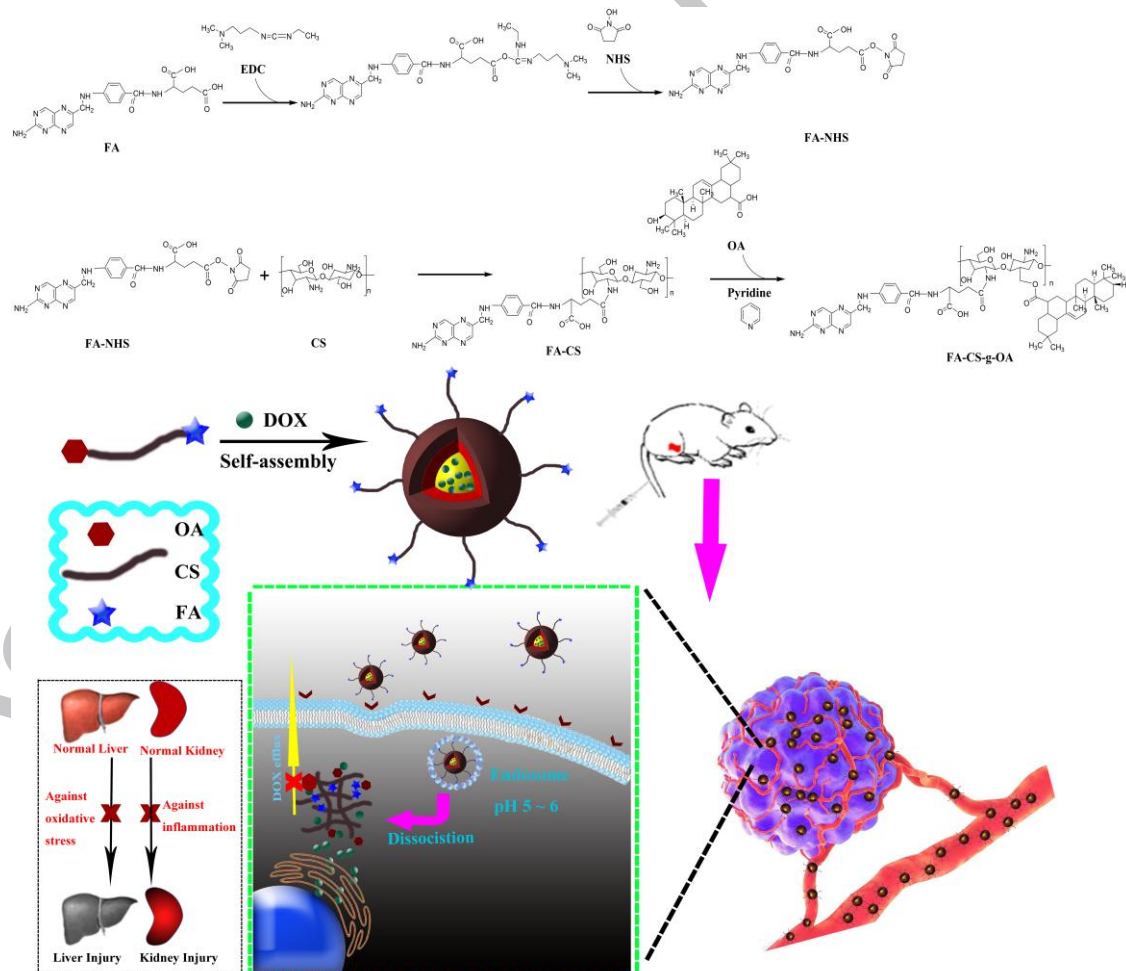
Scheme 1. Schematic illustration of the preparation, microstructure, and application of the FA-CS-g-OA@DOX NPs.

2. Materials and methods

2.1 Materials

CS was purchased from the Sino Pharm Chemical Reagent Co., Ltd (Shanghai, China), with a deacetylation degree of 95 % and average molecular weight (M_W) of 100 kDa. 4-(dimethyl-amino) pyridine (DMAP), pyridine, 1-(3-dimethylaminopropyl)-3-ethylcarbodiimide hydrochloride (EDC·HCl), *N*-hydroxysuccinamide (NHS), 3-(4,5-dimethyl-thiazol-yl)-2, 5-diphenyltetrazolium bromide (MTT), calcein-AM, propidium iodide (PI), OA and phosphate buffered saline (PBS) were purchased from Sigma-Aldrich (St. Louis, MO, USA). FA (M_W=441 Da) was supplied by Wako Pure Chemical Industries, Ltd. (Osaka, Japan). DOX ($C_{27}H_{29}NO_{11}HCl$, 98%) and dialysis tubing were purchased from Shanghai Yuanye Biotech Co., Ltd. (Shanghai, China). Dulbecco's Modified Eagle Medium (DMEM), fetal bovine serum (FBS), penicillin, streptomycin, and trypsin–EDTA were obtained from Gibco (Carlsbad, CA, USA). 4',6-diamidino-2-phenylindole (DAPI) was purchased from Dingguochangsheng Biotechnology Co. Ltd. (Beijing, China). DiR (1,10-dioctadecyl-3,3,30,30-tetramethylindotricarbo cyanine iodide) was procured from Biotium (Hayward, CA, USA). Tween-20, TUNEL and Ki67 commercial detection kits were obtained from Beyotime (Beijing, China). P-gp, MRP1, PARP, PTEN, p53, MMP-2, TGF-β, Collagen I and β-actin antibodies were purchased from Cell Signaling Technology (Danvers, MA, USA). Deionized water, used throughout the research work, was produced using a Milli-Q Gradient A10 System (Merck Millipore, Burlington, MA, USA). All chemicals were used as obtained without any further purification.

2.2. Cell lines and culture procedures

The human breast adenocarcinoma cell line (MDA-MB-231) and the control HUVEC cell line were kindly provided by the Chinese Academy of Sciences (Shanghai, China). All cells were cultured in DMEM supplemented with 10% (v/v) FBS and 1% (v/v) penicillin-streptomycin in a humidified atmosphere of 95% air and 5% CO_2 at 37 ℃.

2.3. Animals and the murine xenograft MDA-MB-231 tumor model

All animal care and handling was conducted in accordance with the Guide for the Care and Use of Laboratory Animals published by the US National Institutes of Health (NIH Publication No. 8523, revised 1985). All experimental protocols were approved by the Animal Care and Use Committee of Kunming Medical University (reference: KMMU 2015002).

Adult male Sprague-Dawley rats (180-200 g, 3-4 weeks old) were obtained from the

Kunming Medical University (Kunming, China), and raised with free access to food and water under specific pathogen-free conditions in a room maintained under a 12 h light/dark cycle. For tumor models, female nude mice (16-20 g, 5-6 weeks old) were supplied by the Animal Center of Kunming Medical University (Kunming, China) and housed under specific pathogen-free conditions with free access to standard food and water. The temperature was maintained at 20-22 ℃. Tumor-bearing xenografts were established by subcutaneous inoculation of 5×10^6 MDA-MB-231 cells (150 μL) into the right flank of each mouse. The tumor sizes of all mice were monitored with a digital caliper and tumor volume calculated using the formula $V_{tumor} = LW^2/2$ (L: tumor length, W: tumor width). When the tumor reached a designated volume (100 mm^3), the mice were randomly grouped for experiments.

2.4. Synthesis of FA-CS-g-OA@DOX NPs

The route of FA-CS-g-OA@DOX NP preparation is illustrated in Scheme 1. Firstly, the FA-CS conjugate was prepared as previously described [29]. A mixture of FA, EDC and NHS (1.0 M, molar ratio 1 : 1 : 1) was prepared in 15 mL anhydrous DMSO, and continuously stirred at room temperature until FA was fully dissolved (ca. 1 h). Thereafter, the activated FA was slowly added to a 1.0 % (w/v) solution of CS (5.0 g in 500 mL of acetate buffer (pH 4.7)). The resulting mixture was stirred at room temperature overnight in the dark. The product was dialyzed against 1.0 mM aqueous NaOH with a 3,500 Da molecular weight cutoff (MWCO) membrane for 72 h to remove unreacted FA. Finally, the resultant FA-CS was isolated by lyophilization.

Subsequently, OA was grafted to FA-CS *via* an esterification reaction. Briefly, 0.50 g of FA-CS was dissolved in 12 mL of pyridine in the presence of DMAP (0.05 g), and 0.90 g OA was added. The molar ratio of OA -COOH groups to FA-CS -OH groups was 2:1. The reaction was kept at room temperature for 3 h and then the solvent evaporated under reduced pressure. The precipitate was dissolved in acetone, and washed three times with water (3×5 mL). The resultant solid FA-CS-g-OA was then collected (yield 1.02 g, 72.9%). Analogous CS-g-OA particles were prepared by reacting OA with non-functionalized CS.

The FA-CS-g-OA and CS-g-OA NPs were seen to self-assemble to nanospheres in an aqueous medium, and the antitumor drug DOX was loaded via the solvent dialysis method. In this, freeze-dried NPs (100 mg) and DOX (20 mg) were dissolved in DMSO (10 mL), sealed in a dialysis bag with a 8,000-10,000 Da Mw cutoff, and dialyzed against water for 48 h at 25 ℃. The

resultant suspension was centrifuged at 6,000 rpm for 30 min to remove any unencapsulated drug.

2.5. Characterization of NPs

The mean diameters, polydispersity indices (PDI) and zeta potentials (ZP) of CS, FA-CS, FA-CS-g-OA, and FA-CS-g-OA@DOX NPs were determined on a Zetasizer Nano ZS90 instrument (Malvern Instruments, Westborough, MA, USA) using a dynamic light scattering (DLS) method. Measurements were performed in triplicate in three independent experiments. For structure confirmation, Fourier transform infrared (FT-IR) spectra were recorded on a Nicolet Nexus 670 spectrometer (Thermo Fisher, Waltham, MA, USA) using powdered NPs (ca. 2 mg) dispersed in KBr (ca. 200 mg). Scans were recorded over the range 3500–1125 cm^{-1} with a resolution of 2 cm^{-1} and 64 scans taken per sample. ^{1}H NMR measurements were performed on a DRX 400 nuclear magnetic resonance spectrometer (Bruker, Faellanden, Switzerland) using D_2O or d6-DMSO as the solvent. Ultraviolet (UV) spectra were measured using a UV-2012 spectrophotometer (UNICO, Shanghai, China). The morphologies of the FA-CS-g-OA@DOX NPs were examined using a scanning electron microscope (SEM; Nova TM Nano SEM, FEI, Hillsboro, OR, USA) and transmission electron microscope (TEM; JEM 1200EX, JOEL, Tokyo, Japan). For TEM experiments, a drop of dispersed NPs was placed onto a carbon-coated grid, and the excess removed. Phosphotungstic acid hydrate (0.5 %, 10 μL) was then added, followed by air drying for 30 min. Thermogravimetric analysis (TGA) was performed using a DTG-60H analyzer (Shimadzu, Kyoto, Japan).

To determine the percentage encapsulation efficiency (EE) and drug loading (DL) of DOX in FA-CS-g-OA@DOX, a dispersion of the NPs was digested with DMSO (100 mL). After centrifugation to precipitate any solid material, the amount of unencapsulated drug in the supernatant was determined by UV/vis spectroscopy. The DOX concentration was determined with reference to a pre-determined calibration curve. The EE and DL were calculated as follows:

$\%EE = (DOX_t - DOX_f) / DOX_t \times 100 \%$

$\%DL = (DOX_t - DOX_f) / \text{Total weight of NPs} \times 100 \%$

where DOX_t is the total amount of DOX used in the preparation of NPs and DOX_f is the amount of unencapsulated DOX present in the supernatant.

2.6. In vitro *drug release*

To evaluate DOX and OA release from FA-CS-g-OA@DOX NPs, a 3 mL suspension of

FA-CS-g-OA@DOX NPs (3 mg) in water was placed into a dialysis bag (MWCO =14,000 Da), and the latter placed in a release medium comprising 0.1 M PBS (5 mL) at pH 5.0, 6.5 or 7.4. Release experiments were conducted under shaking at a speed of 100 rpm at 37 °C. At predetermined time intervals, 1 mL of the PBS solution was withdrawn, and an equal volume of fresh preheated buffer solution was added into the release system. The amount of DOX or OA in the supernatant was determined using UV-vis spectroscopy.

2.7. In vitro *cytotoxicity and antitumor activity*

The cytotoxic effects of FA-CS-g-OA@DOX NPs were evaluated using the MTT assay with MDA-MB-231 cells. HUVEC cells were employed as a control. Both cell types were initially grown in culture flasks with DMEM medium containing 10% v/v fetal bovine serum, penicillin (100 U/mL), and streptomycin (100 mg/mL). Cells were harvested for subculture every three days with 0.25% trypsin solution.

For MTT experiments, 10^5 cells/well (180 μL) were seeded into a 96-well plate and incubated for 24 h (5% CO_2, 37 °C). The various formulations (DOX, OA, FA-CS-g-OA and FA-CS-g-OA@DOX) were then added (giving final DOX concentrations ranging from 0.001 to 10 μg/mL; the OA concentrations are one third of the DOX concentrations). The cells were then incubated in an atmosphere containing 5% CO_2 at 37 °C. The MTT reagent (5 mg /mL, 20 μL per well) was added 24 h later and the plate incubated for a further 4 h. Finally, the MTT solution was removed and DMSO (150 μL) added to the wells. The absorbance was measured at 570 nm using a microplate reader (PowerWave XS, Bio-Tek, Winooski, VT, USA). Three independent experiments were performed with five replicate wells per experiment.

The *in vitro* antitumor activity of the FA-CS-g-OA@DOX NPs was assessed with a calcein-AM/PI double-labeling method. MDA-MB-231 cells were seeded in six-well plates (2 mL, 5×10^5 cells/well) and incubated overnight at 37 °C to allow the cells to adhere. The medium was then aspirated and an NP suspension (50 mg/mL, 200 μL) in DMEM added. After treatment for 6 h, cells were washed with PBS three times and then cultured in DMEM for a further 24 h. The cells were subsequently stained with a mixed Calcein-AM and PI solution for 10 min. Apoptotic cells (red) and living cells (green) were imaged under an inverted fluorescent microscope (Nikon TE-2000U, Tokyo, Japan).

2.8. Molecular level evaluation of apoptosis

To examine the pro-apoptotic effect of FA-CS-g-OA@DOX NPs on tumor cells in depth, a molecular level evaluation of apoptosis was performed using the real-time reverse transcriptase polymerase chain reaction (RT-qPCR). MDA-MB-231 cells were harvested after being incubated with PBS, DOX, OA, FA-CS-g-OA and FA-CS-g-OA@DOX using the same conditions as for the MTT experiments. The total RNA was isolated from the cells using the Trizol reagent (Invitrogen, Carlsbad, CA, USA) according to the manufacturer's instructions. One microgram of total RNA from each sample was used for reverse transcription in a 25 μL reaction volume, following the vendor's instructions. 1 μL of each cDNA was used for PCR in a 20 μL reaction. PCR cycling conditions were: 40 cycles of 94 ℃ for 1 min, 60 ℃ for 1 min, and 72 ℃ for 2 min. One representative anti-apoptotic gene (*Bcl-2*) and three pro-apoptotic genes (*Bax, Caspase-3, Caspase-9*) were selected for determination at the messenger RNA (mRNA) level. The primers used for PCR were: *Bcl-2* forward primer 5'-GACTGAGTACCTGAACCGGC-3' and reverse 5'-TCACTTGTGGCCCAGGTATG-3', product length 190 bps; *Bax* forward primer 5'-CTGGATCCAAGACCAGGGTG-3' and reverse 5'-GTGAGGACTCCAGCCACAAA-3', product length 145 bps; *Caspase-3* forward primer 5'-AGCTTGGAACGGTACGCTAA-3' and reverse 5'-CCACTGACTTGCTCCCATGT-3', product length 145 bps; *Caspase-9* forward primer 5'-CACCTTCCCAGGTTGCCAAT-3' and reverse 5'- CAAGCCATGAGAGCTTCGGA-3', product length 156 bps; and *GAPDH* forward primer 5'- GGAGAGTGTTTCCTCGTCCC-3', and reverse 5'-ATGAAGGGGTCGTTGATGGC-3', product length 136 bps (T_m 60 ℃). The fluorescence signal was determined at the end of each cycle and the results analyzed with the $2^{-\Delta\Delta CT}$ method.

2.9. Confocal laser scanning microscopy (CLSM) and flow cytometry

The uptake of FA-CS-g-OA@DOX NPs and NPs without FA (CS-g-OA@DOX) by breast tumor MDA-MB-231 cells and control HUVEC cells were analyzed with CLSM and flow cytometry. Cells were maintained in a 5% CO_2 atmosphere at 95% relative humidity and 37 ℃, and detached after reaching 70–80% confluence. For CLSM work, cells were seeded on culture slides (with 1×10^5 cells in 2 mL medium added per well of a 24-well plate) and incubated for 24 h at 37 ℃. Free DOX solutions (dissolved in 1% DMSO, 99 % PBS) or FA-CS-g-OA@DOX NP suspensions (dispersed in PBS) were prepared at 50 μg/mL DOX concentration, then 1 mL of a DOX-containing medium added per well. After incubation for 2 h, the cells were washed with

PBS (pH 7.4) three times and fixed with a 4% (v/v) aqueous formaldehyde solution for 10 min. The nuclei were then stained with DAPI (100 mg/mL, 80 μL/well), and the cells were examined by CLSM (FV1000, Olympus, Tokyo, Japan).

For flow cytometry, after the incubation with free DOX or FA-CS-g-OA@DOX NPs, the cells were collected, washed three times with PBS and then resuspended in PBS (1×10^6 cells/mL). Flow cytometry was performed on a Accuri C6 instrument (Beckton-Dickson, Franklin Lakes, NJ, USA). 10,000 events were collected for each sample.

2.10. In vitro *hemolysis assay*

Hemolytic activity was assessed in order to determine the pharmacological safety of the NPs using rat red blood cells (RBCs) collected on heparin. Blood was obtained from male Sprague-Dawley (SD) rats and red blood cells (RBCs) were separated by centrifuging the blood at 1,500 rpm for 15 min. RBC were then resuspended in cold saline at a 2 % (w/v) concentration. DOX, OA, FA-CS-g-OA and FA-CS-g-OA@DOX were serially diluted to different concentrations and incubated with the RBCs for 30 min or 120 min at 37 ℃. Intact RBCs were subsequently separated by centrifugation (1500 rpm, 10 min) and the supernatant was collected. The amount of hemoglobin release was determined by reading the absorbance at 540 nm in a microplate reader (PowerWave XS, Bio-Tek, Winooski, VT, USA). The controls for zero (blank) and 100% hemolysis were comprised of RBCs suspended in PBS and 1% w/v Triton X-100, respectively. Each experiment was conducted in triplicate.

2.11. In vivo *pharmacokinetic study*

The pharmacokinetics of DOX or OA release from FA-CS-g-OA@DOX NPs were evaluated in male SD rats (200-220 g). Rats were fasted overnight, with free access to water, before the experiment. All experimental protocols were approved by the Animal Care and Use Committee of the Kunming Medical University. Free DOX (dissolved in 1% v/v DMSO in PBS) or PBS suspensions of FA-CS-g-OA@DOX (7.5 mg DOX equiv. kg^{-1}) were administered by intravenous injection through the tail vein. Blood was collected from the ocular vein at predetermined time points (0, 5, 30 min; 1, 2, 3, 4, 8, 12, 16, 20 and 24 h). The blood samples were centrifuged at 12,000 rpm for 15 min at 4 ℃ and aliquots (100 μL) of the supernatant stored at -70 ℃. The concentration of DOX in the blood was then determined as reported in the literature [30].

2.12. In vivo *biodistribution*

In order to monitor release from the NPs, *in vivo* drug distribution in female nude mice bearing MDA-MB-231 tumors was studied using a Maestro™ *in-vivo* imaging system (CRi Inc., Woburn, MA, USA). The model fluorescent molecule DiR was loaded into FA-CS-g-OA NPs following the same protocol as for DOX loading. When the size of tumors reached approximately 100 mm^3, the mice were intravenously (*i.v.*) injected with either free DiR (in 10 μL DMSO; 7.5 mg DiR equiv. kg^{-1}) or FA-CS-g-OA@DiR NPs (in 10 μL saline; 7.5 mg DiR equiv. kg^{-1}). Fluorescent scans were then performed at various time points (1, 4, 8, 12, 24 and 48 h) post *i.v.* injection [31]. After *in vivo* imaging, the mice were sacrificed and the tumor, liver, kidney, lung, spleen and heart were removed and collected for further *ex vivo* fluorescence imaging of DiR.

2.13. In vivo *antitumor efficacy*

150 μL of a MDA-MB-231 cell suspension (ca. 5×10^6 MDA-MB-231 cells) was subcutaneously injected into the right flank area of the nude mice. When the tumor volume reached approximately 100 mm^3, the mice were randomly divided into 5 groups (8 mice per group) and treated with saline, DOX, OA, FA-CS-g-OA and FA-CS-g-OA@DOX (7.5 mg/kg DOX equiv.) via *i.v.* injection every two days. The tumor sizes of the mice were monitored with a digital caliper and the volume calculated as $V_{tumor} = L \times W^2/2$ (L: tumor length, W: tumor width). After each injection, the weight of each mouse was determined. The survival time of each mouse was also recorded and evaluated by Kaplane-Meier analysis [32].

2.14. Histological and immunohistochemical examinations

At the end of the treatment (day 30), one mouse from each group was sacrificed. The tumor and major organs were excised, fixed with paraformaldehyde for 48 h, embedded in paraffin, and cut into 5 mm thin slices. To observe cell apoptosis in the tumor tissue, it was further sliced into thin sections and stained with a terminal deoxynucleotidyl transferase dUTP nick end labeling (TUNEL) apoptosis detection kit. The tumor tissue sections were also subjected to Ki67 analysis for determining the inhibition rate of tumoral proliferation, using a commercial detection kit according to the manufacturer's instructions. For histological examination, tumor tissues and organs sections were stained with hematoxylin and eosin (H&E) and observed with an optical microscope.

2.15. Cytokine detection.

All remaining mice were sacrificed on day 31 after fasting overnight [33]. Blood samples

were collected *via* heart puncture, with the animals under terminal anesthesia using 0.01 mg/kg phenobarbital (Kefeng Chemical Reagent Co., Shanghai, China). These blood samples were then centrifuged (3,500 rpm, 15 min, 4°C) to obtain the serum. The concentrations of hepatic function indices (alanine aminotransferase (ALT) and aspartate aminotransferase (AST)), and renal function indices (creatinine (Scr), urea nitrogen (BUN)) in the serum were measured using an automated AU5400 biochemistry analyzer (Olympus, Tokyo, Japan). In addition, serum levels of the inflammatory cytokines interleukin-6 (IL-6), interleukin-1β (IL-1β) and tumor necrosis factor-α (TNF-α), together with oxidative stress biomarkers (glutathione peroxidase (GSH-Px), malondialdehyde (MDA), and superoxide dismutase (SOD)) were determined using commercial ELISA kits (Bioswamp, Shanghai, China). All procedures complied with the manufacturer's instructions.

2.16. Western blot analysis

The tumors from the xenograft nude mice were excised and washed with physiological saline, then homogenized in modified RIPA buffer supplemented with 1:100 (v/v) of a proteinase/phosphatase inhibitor cocktail (Solarbio, Beijing, China). Insoluble material was removed by centrifugation at 12,000 g and 4 °C for 30 min. Protein content was then determined with a commercial BCA kit (Beyotime, Beijing, China). Subsequently, equal amounts of 40 μg total protein were loaded per lane on a 10% SDS–PAGE gel for separation. After SDS-PAGE, the proteins were transferred to polyvinylidene difluoride (PVDF) membranes, preincubated in blocking solution at room temperature for 2 h, and incubated with the primary antibodies for P-gp (1:500), MRP1 (1:500), poly(ADP-ribose polymerase) (PARP, 1:1000), phosphatase and tensin homolog (PTEN, 1:100), p53 (1:100), matrix metalloproteinase-2 (MMP-2, 1:800), transforming growth factor (TGF-β, 1:800), collagen I (1:500) and β-actin (1:2000, Santa Cruz, Dallas, TX, USA) overnight at 4 °C. After being washed three times for 10 min with Tris-buffered saline containing 0.5% Tween-20, the membrane was incubated with the corresponding secondary antibody linked to horseradish peroxidase (goat antimouse IgG, 1:10,000; Santa Cruz, Dallas, TX, USA) for 2 h at room temperature. Immunoreactive proteins were visualized using Super Signal West Pico Chemiluminescent Substrate (Thermo Scientific, Rockford, IL, USA). Finally, membranes were treated with an enhanced chemiluminescent reagent (Merck Millipore, Burlington, MA, USA) and exposed to a Kodak X-Omat film (Kodak, Xiamen, China). After the

film was developed the intensity of immunoreactivity was measured by densitometry within the ImageJ software (National Institutes of Health, Bethesda, MD, USA).

2.17. Statistical Analysis

Statistical analysis was conducted using the Student's *T* test for comparison of two groups and one-way ANOVA for multiple groups, the latter followed by a Newman-Keuls test if the overall $P < 0.05$. A P value of less than 0.05 was considered significant (*), while a P value of less than 0.01 was considered highly significant (**).

3. Results and discussion

3.1. Preparation and characterization of FA-CS-g-OA@DOX NPs

FT-IR spectra of CS, OA, FA and the FA-CS-g-OA copolymer are shown in Fig. 1A. The absorption bands at 1025 and 1062 cm^{-1} can be ascribed to the C$_6$–OH and C$_3$–OH of the CS. Compared with CS (black), FA-CS-g-OA (pink) shows a reduction in the intensity of the primary NH$_2$-associated band at 1689 cm^{-1} and the appearance of a new NH-associated band at 1645 cm^{-1}, consistent with Amide II vibrations. In addition, a new band at 1396 cm^{-1} is visible in FA-CS-g-OA, which was attributed to C–N bonds in a secondary amine (from FA). Hence, it is clear that the NH$_2$ groups in CS were partly converted into NH groups after the reaction between FA and CS.

The successful introduction of FA and the OA onto CS was also explored by ^{1}H NMR spectroscopy. The spectrum of the composite (Fig. 1B) contains signals originating from both FA, CS and OA (the full set of spectra are shown in the Supplementary Information, Fig. S1), displaying peaks from the protons on the carbon backbone of CS (at 3.00–4.00 ppm), as well as distinct resonances from FA. The peak at 8.65 ppm is particularly notable and corresponds to the proton of the pterin ring of FA; additional peaks at 7.69 and 2.53 ppm are characteristic signals of the benzene ring and methylene of FA, respectively. Resonances in the spectrum of FA-CA-g-OA at 5.3 ppm and 0.7–2.0 ppm were assigned to the protons of OA. Due to the formation of ester bonds between OA and CS, the proton peak δ 3.2 (1H, t) of OA moves to δ 4.2 (1H, t) in FA-CA-g-OA, further indicating its successful synthesis.

DOX was then loaded into FA-CS-g-OA by shaking a mixture of DOX and FA-CS-g-OA in DMSO for 24 h. The UV spectra of CS, FA, FA-CS-g-OA and FA-CS-g-OA@DOX were collected in 0.2 M PBS solution (pH 7.4) and are depicted in Fig. 1C. The characteristic

absorbance of DOX (absorbance max: 484 nm) was visible for the FA-CS-g-OA@DOX NPs, indicating the successful loading of DOX into FA-CS-g-OA. In addition, the presence of the FA moiety was confirmed by the UV spectrum of the FA-CS-g-OA@DOX NPs showing the characteristic FA absorption peak at 293 nm. These data, along with the findings of FT-IR and ^{1}H NMR, confirm that the FA-CS-g-OA@DOX NPs were successfully prepared.

The morphologies of the FA-CS-g-OA@DOX NPs were investigated by SEM and TEM (Fig. 1D, E), and the NPs are found to have a spherical structure with uniform sizes of ~ 90 nm. DLS and zeta potential analysis was also performed to investigate the size and surface charge of the nanocomposites during the preparation process. As expected, an increase in size after subsequent surface modifications is observed, and reflects the successful addition of FA and OA (see Supplementary Information, Fig. S2). The size of the FA-CS-g-OA@DOX NPs in aqueous suspension is larger (180 nm, PDI: 0.245) than seem by electron microscopy (Fig 1D, E cf. Fig. S2), as a result of the NPs being hydrated [34].

The surface charge varied after each step of the conjugation, from $+30.9 \pm 0.5$ mV for CS (as a result of the amine groups) to $+15.4 \pm 0.3$ mV after FA modification (because some of the amine groups are converted to amides, and there are COOH groups on FA), and then to -10.3 ± 0.2 mV after subsequent OA grafting. The hydrodynamic sizes of all the NPs are below 200 nm and they have a narrow size distribution (PDI <0.45), which is appropriate for tumor targeting by the EPR effect. This size distribution is also suitable for intravenous administration. The FA-CS-g-OA@DOX NPs further exhibited a constant size upon storage as an aqueous suspension for 7 days, indicating a good stability to aggregation (Supplementary Information, Fig. S2E). UV analysis indicated that the DL of DOX was $15.6 \pm 1.9\%$ and EE was $85.3 \pm 9.7\%$. The OA content is calculated at 5.1% w/w from TGA data (Fig. S3). These relatively high values (notably higher than several CS NPs previously reported [35, 36]) indicate that the FA-CS-g-OA@DOX NPs are suitable for the delivery of antitumor drugs.
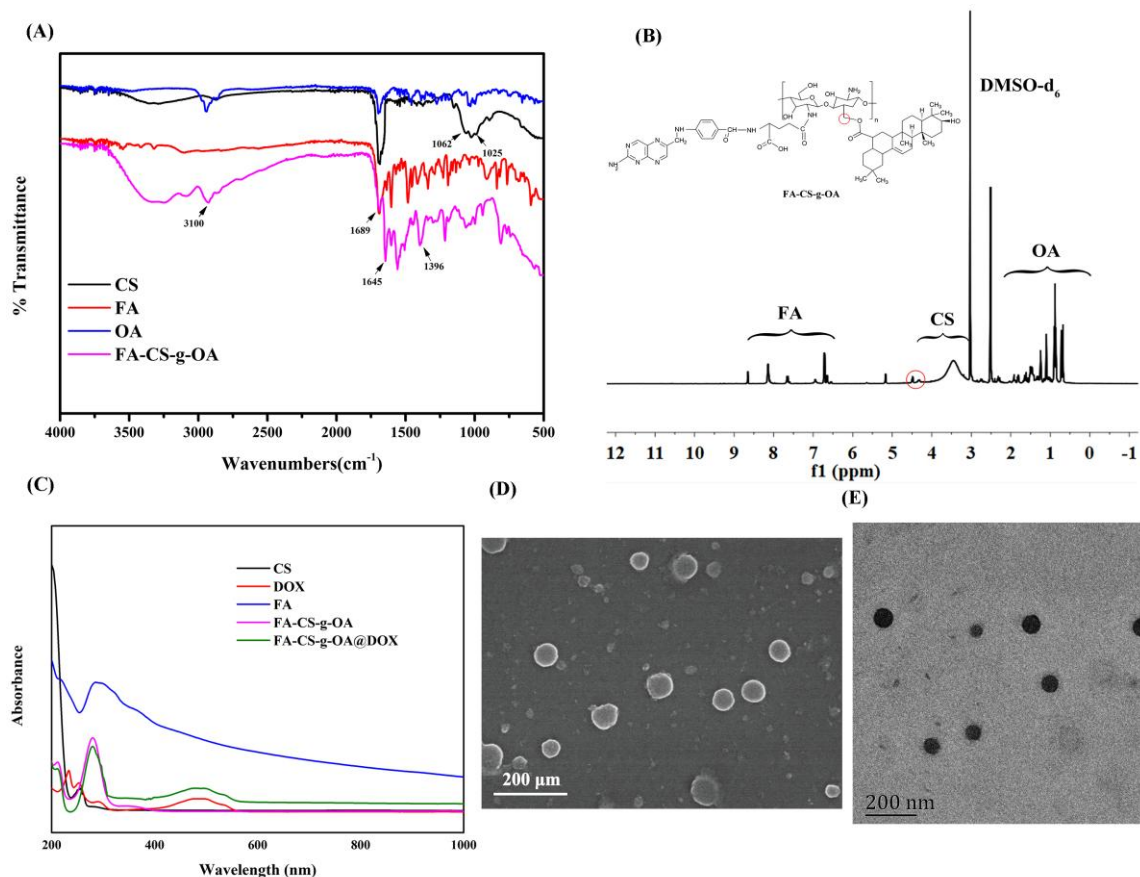
Fig. 1. Synthesis and characterization of FA-CS-g-OA@DOX NPs. (A) FT-IR spectra of CS, FA, OA, and FA-CS-g-OA. (B) ^{1}H NMR spectrum of FA-CS-g-OA in DMSO-d_6. (C) UV spectra. Representative (D) SEM and (E) TEM micrographs of FA-CS-g-OA@DOX NPs are also given.

3.2. In Vitro *drug release study.*

The extracellular fluid in the tumor tissue (pH = 6.5-7.2) is more acidic than that in normal tissue (pH~7.4), while intracellular endosomes and lysosomes (pH = 4.5-6.5) also possess acidic environments [37]. Therefore, the *in vitro* drug release study of FA-CS-g-OA@DOX NPs was determined at different pH values to mimic relevant *in vitro* environments: 1) physiological tissue (pH = 7.4); 2) the extracellular fluid of a tumor (pH = 6.5); and, 3) the endosome-lysosome in carcinoma cells (pH = 5.0). The results for DOX release are presented in Fig. 2A. It is clear that pH has a major effect on drug release from the FA-CS-g-OA@DOX NPs. DOX was quickly released at pH 5.0, reaching ca. 90 % in the first 24 h, after which it slows. In contrast, only ~ 35 % of the DOX loading was released after 48 h at pH 7.4. The pH 6.5 experiment is intermediate between these extremes. These effects can be attributed to the increased ionization, and thus solubility, of CS at reduced pHs.

The release profiles of OA from FA-CS-g-OA@DOX NPs follow a very similar trend (Fig.

2B). The cumulative release percentage of OA after 72 h reached 31.0 ± 3.2 %, 51.8 ± 5.3 % and 76.0 ± 8.2% at pH 7.4, pH 6.5 and pH 5.0 respectively. An acidic milieu can accelerate the release of OA by promoting the hydrolysis of the ester bond connecting OA to CS [38], in addition to the increased solubility of CS at lower pH. The accelerated release of both active ingredients at weakly acidic pHs is very promising for anti-cancer applications.
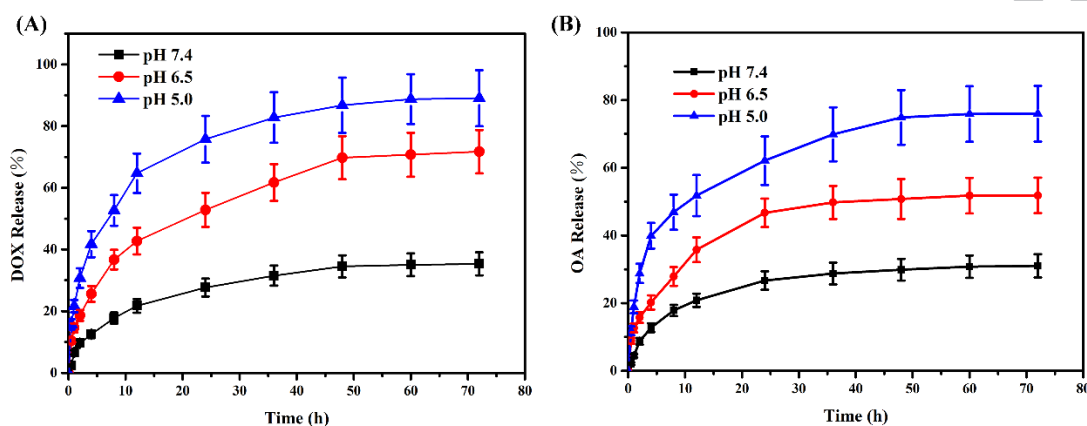

Fig. 2. *In vitro* release profiles of (A) DOX and (B) OA from FA-CS-g-OA@DOX at different pHs. Error bars represent the standard deviation ($n = 3$).

3.3. In vitro *cytotoxicity and antitumor effects*

The *in vitro* anticancer effects of free DOX, free OA, FA-CS-g-OA and FA-CS-g-OA@DOX NPs were evaluated in MDA-MB-231 human breast cancer cells. Healthy HUVEC cells were used to assess the biocompatibility of the various materials. As shown in Fig. 3A, FA-CS-g-OA induced negligible cytotoxicity to normal HUVEC cells at concentrations up to 10 µg/mL (> 90% cell viability). OA is slightly toxic to HUVECs, and induces more cell death than FA-CS-g-OA. DOX and FA-CS-g-OA@DOX do cause the death of HUVEC cells, the latter is less toxic than the former, but not statistically significant ($P > 0.05$, when the concentration of DOX was less than 10 µg/mL), which is promising for selective delivery applications.

All the DOX-containing samples displayed dose-dependent cytotoxicity to MDA-MB-231 cells (Fig. 3B). Relative to free DOX, FA-CS-g-OA@DOX NPs exhibited greater toxicity to MDA-MB-231 cells over the entire concentration range explored (0.001-10 µg/mL) after 24 h of incubation. Similarly, the cytotoxicity of FA-CS-g-OA was higher than free OA. These effects can be explained by a combination of more efficient cellular uptake in the case of the NPs, and the acidic microenvironment of the cellular milieu accelerating drug release from the formulations.

The half maximal inhibitory concentrations (IC_{50}) of free DOX, free OA, FA-CS-g-OA and FA-CS-g-OA@DOX NPs to MDA-MB-231 cells were calculated to be 7.8 ± 0.9 μg/mL, 123.6 ± 11.7 μg/mL, 15.8 ± 1.7 μg/mL and 1.8 ± 0.1 μg/mL, respectively (Fig. 3C). A synergistic enhancement in cytotoxicity to MDA-MB-231 cells is thus obtained through the integration of two therapeutic agents (DOX and OA) within a single platform. These data further confirm the chemosensitizing effect of OA on DOX cytotoxicity as reported in literature [24].

To evaluate whether the inhibition of cell proliferation by FA-CS-g-OA@DOX NPs was due to the induction of apoptosis, cell apoptosis was evaluated by calcein-AM/PI double staining (Fig. 3D). More apoptotic cells were observed upon treatment with FA-CS-g-OA@DOX NPs than with free DOX or OA treatment, confirming apoptosis to be important in the anti-cancer effects of the NPs.

In order to investigate the effect of FA-CS-g-OA@DOX NPs on tumoral cell apoptosis in depth, it was necessary to perform a molecular level evaluation. RT-qPCR was used to detect the mRNA expression levels of several important apoptosis-related genes (*Bcl-2*, *Bax*, *Caspase-3*, and *Caspase-9*) in MDA-MB-231 cells. *Bcl-2* is a vital proto-oncogene and the first confirmed gene able to participate in preventing apoptosis of cells and prolonging cell survival [39]. As shown in Fig. S4A, compared with the PBS control group all drug treatments significantly ($P < 0.05$) inhibited the expression of *Bcl-2* mRNA in breast cancer cells and promoted the process of cancer cell apoptosis. Furthermore, the downregulation effect of the FA-CS-g-OA@DOX NPs was greater than that of other formulations ($P < 0.01$). The *Bax* (an inhibitor of Bcl-2), *Caspase-3* and *Caspase-9* genes (members of the cysteine-aspartic acid protease family) are activated in apoptotic cells both by extrinsic and intrinsic pathways, and were found to be upregulated in MDA-MB-231 cells after incubation with DOX, OA, FA-CS-g-OA or FA-CS-g-OA@DOX NPs (Fig. S4B, C, D). Cells treated with FA-CS-g-OA@DOX NPs exhibited the highest mRNA expression levels for these three pro-apoptosis genes. It is hence clear that FA-CS-g-OA@DOX NPs can induce apoptosis in tumor cells.
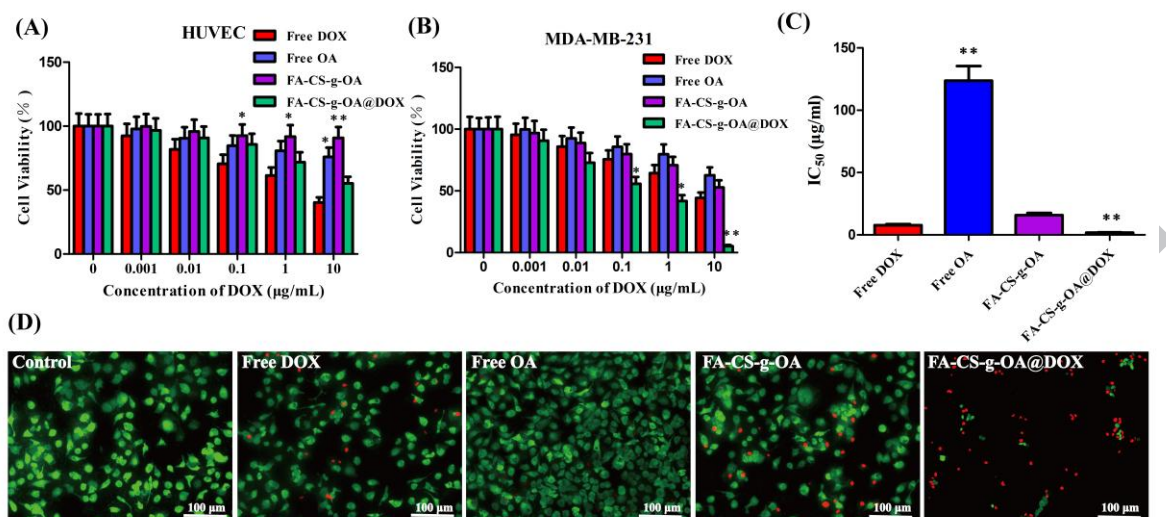
Fig. 3. Cell viability of (A) HUVEC and (B) MDA-MB-231 cells after incubation with DOX, OA, FA-CS-g-OA and FA-CS-g-OA@DOX NPs for 24 h. (C) IC_{50} values against MDA-MB-231 cells for different formulations ($n = 15$; results are shown as mean $\pm$ S.D., $* P < 0.05$, $** P < 0.01$ compared to free DOX). (D) Fluorescence images of calcein-AM (green)/PI (red) double stained cells treated with the different formulations.

3.4. In vitro *cellular uptake*

In vitro cellular uptake experiments were performed using human breast carcinoma MDA-MB-231 cells (known to significantly overexpress the FA receptor), with HUVEC cells (no overexpression of FA receptor) utilized as controls. Cells were incubated with FA-CS-g-OA@DOX NPs or free DOX for 2 h, and then examined by CLSM. As revealed in Fig. 4A, the uptake of FA-CS-g-OA@DOX NPs by MDA-MB-231 cells was noticeably higher than those cultured with free DOX. For HUVEC cells, minimal fluorescence was observed regardless of whether they were treated with FA-CS-g-OA@DOX NPs or free DOX. Moreover, the red fluorescence which can be seen in the cytoplasm in MDA-MB-231 cells is greater and more closely situated around the nuclei (blue) than that in the control HUVEC cells. The main reason for this is that far fewer FA receptors are expressed on HUVEC cells than on MDA-MB-231 cells, resulting in much reduced receptor-mediated endocytosis in the former case.

The specific targeting ability of the FA receptor by FA-CS-g-OA@DOX NPs was further verified by a competitive inhibition assay, in which MDA-MB-231 cells were pretreated with free FA (to saturate the FA receptors on the cell surface) before being cultured with FA-CS-g-OA@DOX NPs or DOX. A sharply decreased uptake of the NPs is observed (Fig. 4A). In addition, no obvious differences in DOX fluorescence are observed between MDA-MB-231 cells incubated with free DOX and those incubated with the NPs. The FA ligands on the NPs

therefore play an important role in increasing cellular uptake via FA-receptor-mediated pathways.

To provide further evidence, flow cytometry was employed to explore the cellular uptake of the FA-CS-g-OA@DOX NPs. Free DOX and FA-CS-g-OA@DOX NPs were incubated with HUVEC and MDA-MB-231 cells for 4 h and then the cellular uptake of DOX quantitatively investigated. The results (Fig. 4B) are consistent with those from fluorescence microscopy. No significant difference in fluorescence intensity was observed between HUVEC cells incubated with free DOX and FA-CS-g-OA@DOX NPs. However, MDA-MB-231 cells exposed to FA-CS-g-OA@DOX NPs exhibited significantly higher mean fluorescence intensity than those treated with DOX, confirming the NPs are taken up to a greater extent by the cells. This can be explained by a combination of three factors: (1) the EPR effect making it easier for the NPs to enter MDA-MB-231 cells than HUVECs; (2) the active targeting effect of the FA moiety of FA-CS-g-OA@DOX; (3) cellular accumulation of DOX is increased with the NPs because the presence of OA inhibits MRP mediated efflux. The cellular uptake observed here with the FA-CS-g-OA@DOX NPs is notably higher than for other FA functionalized CS systems reported in the literature [40, 41], indicating the significant chemosensitizing effect of OA.
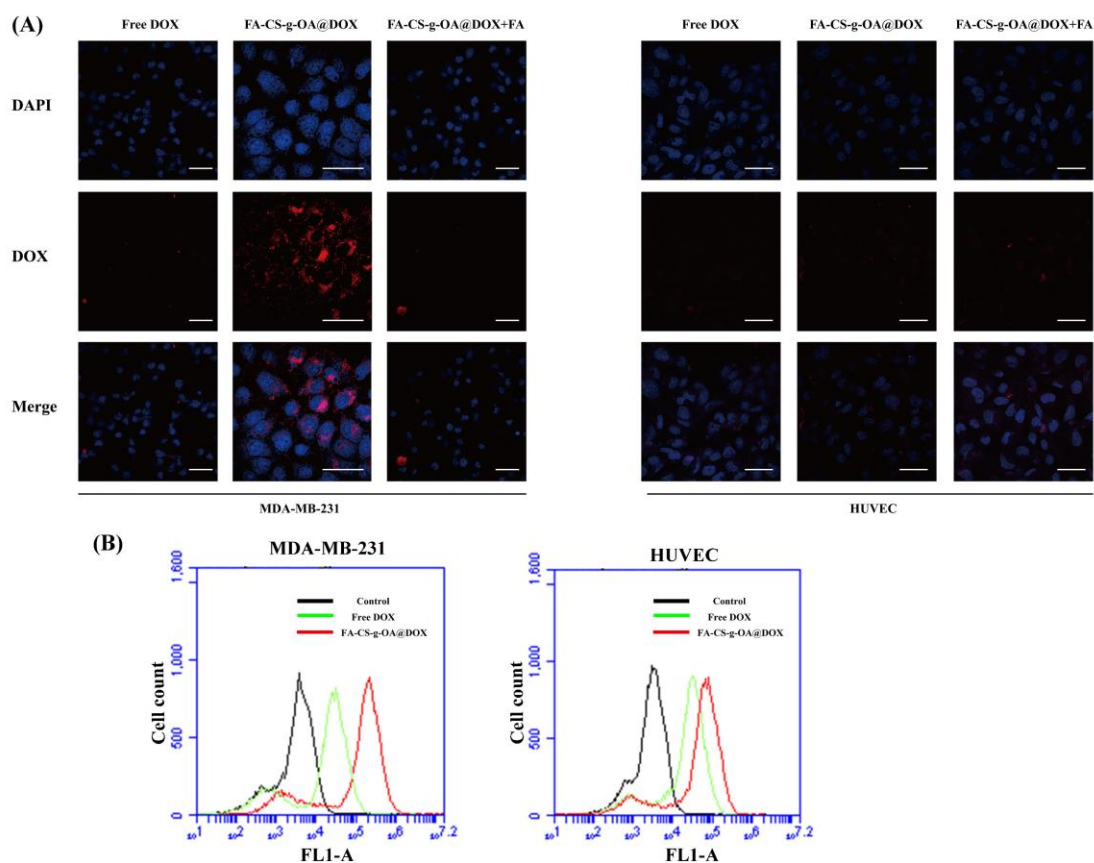
Fig. 4. Cellular uptake assays performed with MDA-MB-231 and HUVEC cells. (A) CLSM data depicting cellular uptake of DOX loaded NPs by MDA-MB-231 and HUVEC cells (all scale bars = 50 μm) and (B) flow cytometry analysis.

3.5. Pharmacokinetics and biocompatibility

The pharmacokinetics of free DOX and FA-CS-g-OA@DOX NPs were studied in SD rats. As can be seen in Fig. 5A, DOX concentrations in the plasma exhibited bi-exponential declines over 24 h. The mean plasma concentrations of the FA-CS-g-OA@DOX NPs were considerably higher than those of the free DOX. Moreover, the AUC, terminal $t_{1/2}$, and MRT values of FA-CS-g-OA@DOX NPs are significantly increased ($P < 0.05$) in comparison to the DOX group. This may arise because of reduced distribution of the FA-CS-g-OA@DOX NPs from the central compartment into tissues and organs. This is thought to be related to the physicochemical properties of NPs (i.e., diameter, zeta potential, and architecture) [34, 42]. The prolonged blood circulation of FA-CS-g-OA@DOX NPs should lead to improved antitumor efficacy.

To explore the biocompatibility of the NPs, a hemolysis assay was conducted to evaluate their compatibility with the blood. The amount of hemoglobin released into solution is directly proportional to the hemolytic activity of the NPs. Almost no visible hemolysis can be observed for

FA-CS-g-OA NPs at concentrations below 250 μg/mL (Fig. 5B). Free DOX induced RBC lysis even at very low concentrations, whereas 250 μg/mL FA-CS-g-OA@DOX NPs had much lower hemolytic activity (< 10 %). Although free OA causes some damage to RBCs, when OA was grafted onto the FA-CS backbone it showed dramatically lower levels of hemolysis. This suggested that FA-CS-g-OA NPs are blood-compatible materials as well as potent drug delivery systems.
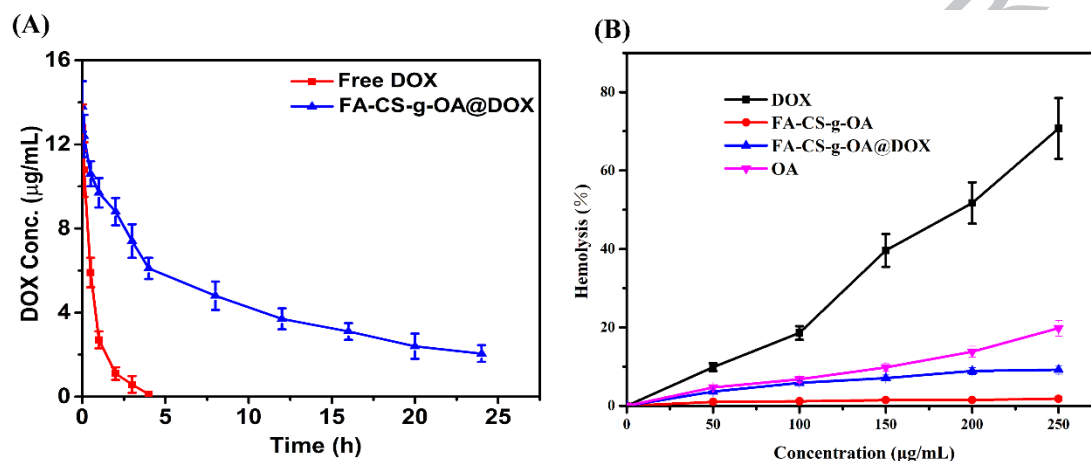

Fig. 5. (A) Plasma concentration *vs* time curve for free DOX and FA-CS-g-OA@DOX in SD rats ($n = 3$, mean ± SD). (B) Hemolytic activity of free DOX, OA, FA-CS-g-OA and FA-CS-g-OA@DOX NPs on rat red blood cells ($n = 3$, mean ± SD).

3.6. In vivo *and* ex vivo *fluorescence imaging*

The real-time biodistribution behavior of free DiR and DiR loaded NPs (FA-CS-g-OA@DiR) was monitored using the living imaging system after intravenous injection into xenografted MDA-MB-231-tumor-bearing mice. A visible signal for DiR was detected in the tumor foci at 4 h after administration of FA-CS-g-OA@DiR NPs (Fig. 6A), the intensity of which increased up to 8 h and was maintained up to 24 h. In comparison, free DiR is distributed much more widely throughout the animal; the presence of DiR in the tumor was barely noticeable at 12 h or earlier, and only after 24 h is a dim fluorescence visible in the tumor area. These findings are probably due to rapid blood clearance within the tumor.

To observe the distribution of DiR more clearly, mice were sacrificed 24 h post-injection, and their hearts, livers, spleens, lungs, kidneys and tumors were harvested for *ex vivo* imaging (Fig. 6B). While DiR in the FA-CS-g-OA@DiR NPs is clearly concentrated in the tumor, with some in the liver, when free DiR is injected it is distributed throughout the body, with noticeable presence in the heat, lungs, liver, spleen and kidneys as well as in the tumor. Quantitative region of interest

(ROI) analysis (Fig. 6C) reveals that the tumors of mice injected with FA-CS-g-OA@DiR NPs exhibited a much higher fluorescence efficiency (2.5-fold greater) than free DiR. These results all show that FA-CS-g-OA@DOX NPs can effectively target and release payloads selectively to a human MDA-MB-231 tumor in mice, due to the combined influence of the EPR effect and FA receptor mediated cell uptake.
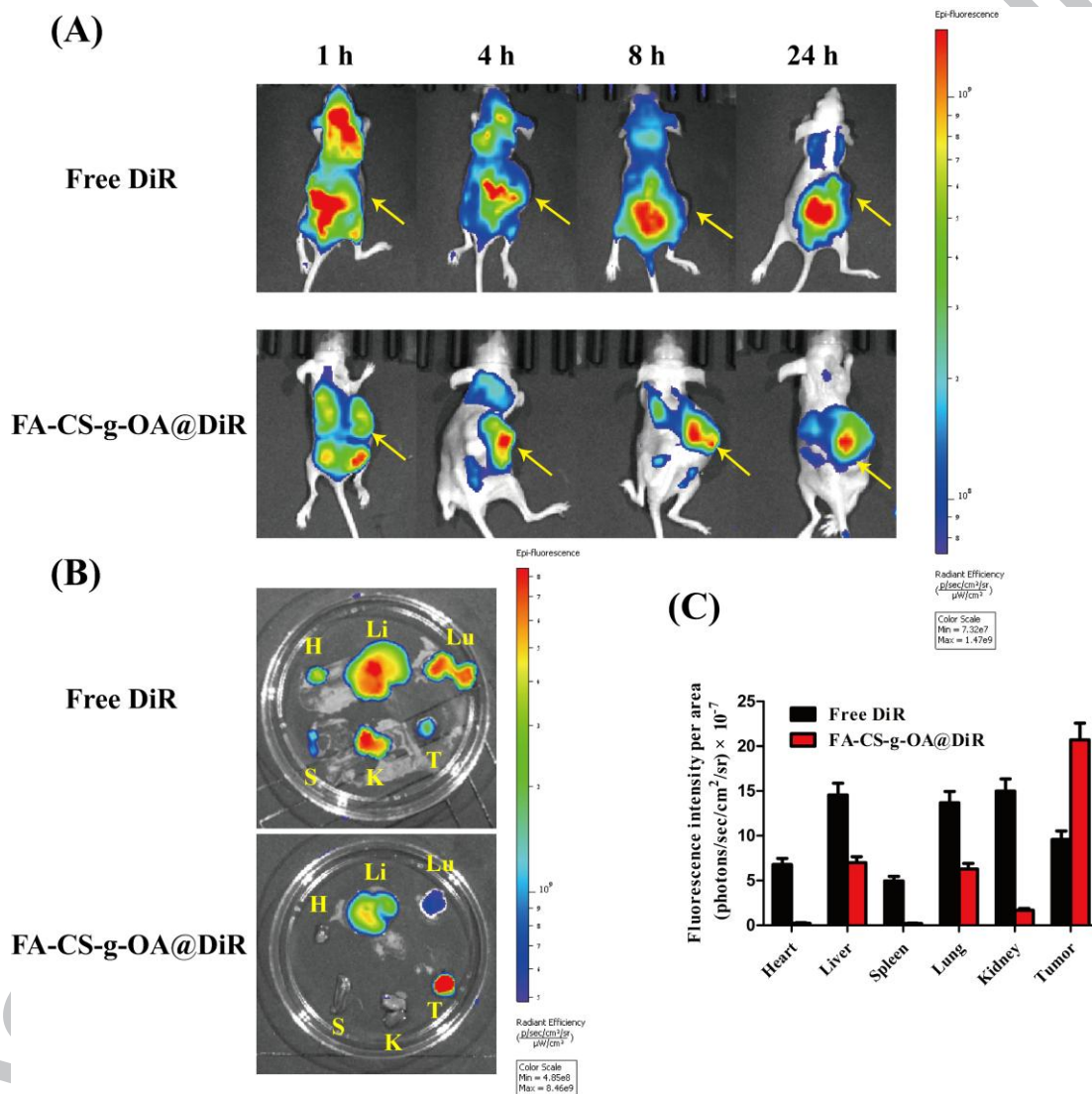

Fig. 6. (A) *In vivo* fluorescence images of MDA-MB-231 xenograft nude mice after *i.v.* injection of free DiR and FA-CS-g-OA@DiR NPs. The arrows indicate the tumor foci of mice. (B) *Ex vivo* distribution and (C) statistical analysis of hearts (H), livers (Li), spleens (S), lungs (Lu), kidneys (K) and tumors (T) harvested after sacrifice (*n* = 3, results are shown as mean ± S.D.).

3.7. In vivo *therapeutic study and safety evaluation*

We further investigated the therapeutic performance of FA-CS-g-OA@DOX NPs using MDA-MB-231 human breast tumor-bearing nude mice. The mice were treated with free DOX,

free OA, FA-CS-g-OA or FA-CS-g-OA@DOX NPs (7.5 mg DOX equiv./kg) after tumors had grown to ca. 100 mm^3 in volume. Mice receiving saline injections were used as a control. After treatment for two weeks, the tumor sizes of the living mice were measured (images given in Fig. S5). It was found that the tumor growth of mice in the FA-CS-g-OA@DOX NP treatment group was significantly inhibited compared to the other groups. No obvious therapeutic benefit was visible with mice treated with free DOX, while the tumor volume of mice treated with either free OA or FA-CS-g-OA also indicated some moderate growth inhibition.

Photographs of excised tumor blocks isolated at day 30 (Fig. 7A) confirmed obvious shrinkage of the tumor after treatment with FA-CS-g-OA@DOX NPs. The tumor is also observed to be smaller upon treatment with free DOX, but this is much less stark than in the case of the FA-CS-g-OA@DOX NP group. Tumor volumes were recorded during the experiment, and as shown in Fig. 7B FA-CS-g-OA@DOX treatment led to very obvious tumor growth inhibition, while the tumor size increased in all other treatment groups. 30 days post-injection, mice treated with saline had average tumor volumes of 746 ± 73 mm^3. FA-CS-g-OA@DOX NPs treatment markedly slowed the growth of tumor tissue, leading to an average tumor volume of 13 ± 2 mm^3 after 30 days. This is a much reduced size than seen in the case of either DOX (251 ± 23 mm^3) or OA (446 ± 43 mm^3).

To investigate the potential tissue toxicity of FA-CS-g-OA@DOX NPs *in vivo*, the body weight of the mice was also periodically monitored (Fig. 7C). With the free DOX group, body weights started to decrease from the 10th day, indicating that DOX had severe side toxic effects. The body weights increased to different degrees after administration of saline, free OA, FA-CS-g-OA and FA-CS-g-OA@DOX NPs. Overall, FA-CS-g-OA and the FA-CS-g-OA@DOX NPs clearly have good biocompatibility in *vivo* and can reduce the toxicity of DOX administration.

The survival time of tumor-bearing mice was evaluated using the Kaplane-Meier test. The survival curves showed that of 75% of mice treated with FA-CS-g-OA@DOX NPs survive over an experimental period of 60 days, while those were given saline or DOX all died within 45 days (Fig. 7D). The free DOX group displayed the lowest survival time, due to its severe toxicity. The survival time of mice treated with FA-CS-g-OA@DOX NPs was significantly higher than that of those receiving free DOX or free OA.

Overall, it is clear that the FA-CS-g-OA@DOX NPs had the highest *in vivo* therapeutic efficacy, without any significant systemic toxicity. This can be attributed to the high biocompatibility of the carrier materials, and both active and passive targeting. In addition, the therapeutic effect of FA-CS-g-OA@DOX NPs appears to be enhanced by the anti-drug resistance effects of OA. This conclusion is further supported by the fact that a better tumor growth inhibition effect was observed for the FA-CS-g-OA@DOX NPs developed in this study than with similar targeting systems without OA developed by our group [7] and others [43, 44].
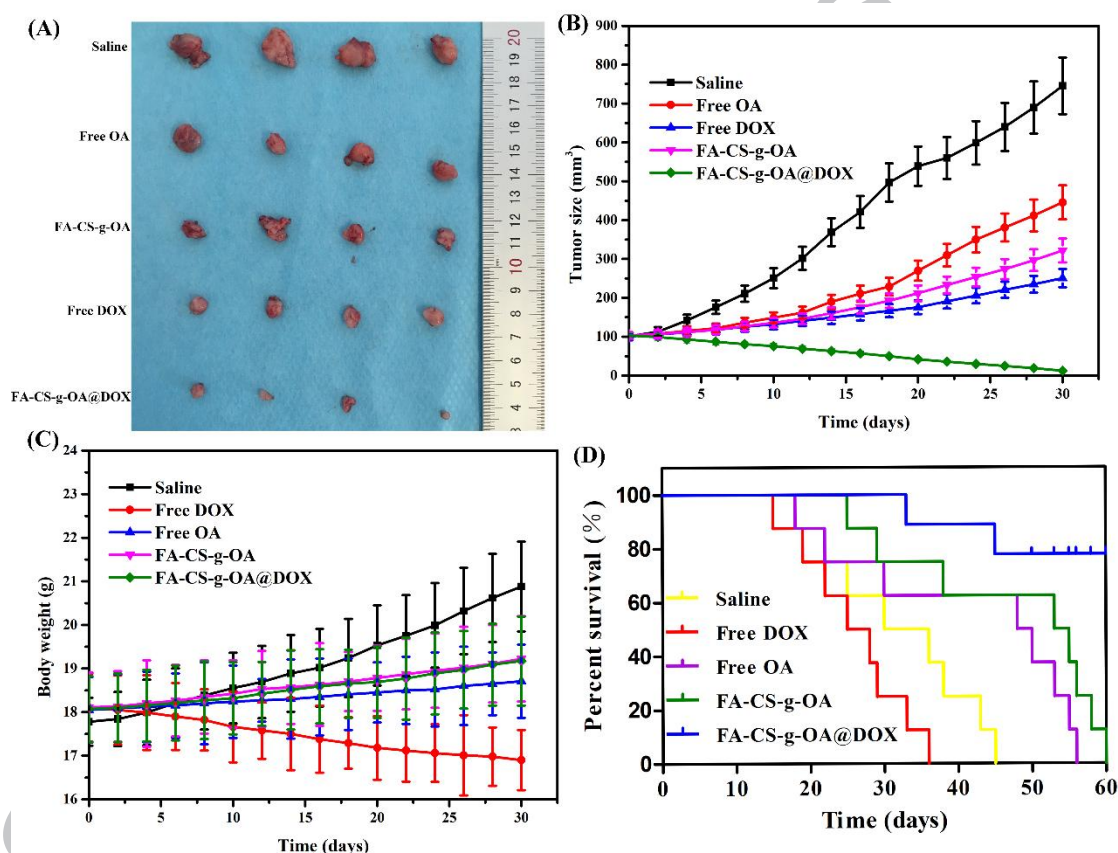

Fig. 7. *In vivo* anti-tumor therapeutic efficacy results. (A) Representative photos of tumor tissues after treatment for 30 days. (B) Real-time measurements of tumor size. (C) Time course average body weights of mice after each treatment. (D) Kaplane-Meier survival curves of tumor-bearing mice.

3.8. Ex vivo *anti-tumor efficacy and systemic toxicity evaluation*

The major organs (heart, liver, spleen, lung and kidney) and tumor were excised from the treated mice after 30 days and imaged using H&E staining. The organ tissue sections (Fig. 8A) revealed no obvious pathological abnormalities, except for the free DOX group. In this case, extensive hepatocellular vesicular steatosis, some focal inflammation of liver, and slight

congestion in the glomerular cells of the kidney can be seen. The FA-CS-g-OA@DOX NPs caused severe necrosis in the tumor tissue, with minimal damage to the liver and no damage observed in the other organs, indicating their selectivity and good histocompatibility [45] [46]. The H&E staining (Fig. 8A) further showed that the area of necrosis in the tumor tissues was larger in the FA-CS-g-OA@DOX NP group than in the other treatment groups. Tissue from tumors in the free DOX and OA treated groups showed many viable tumor cells, confirming that the therapeutic efficacy of FA-CS-g-OA@DOX NPs against MDA-MB-231 tumors is greater than that of DOX and OA. In line with the H&E staining images, statistical analysis of the apoptosis rate in each group (histograms given in Fig. S6) revealed a significantly higher rate in animals treated with FA-CS-g-OA@DOX NPs ($68.7 \pm 6.1\%$) than with free DOX ($45.6 \pm 5.1\%$, $P < 0.05$), free OA ($8.8 \pm 1.0\%$, $P < 0.01$), and FA-CS-g-OA ($25.5 \pm 3.1\%$, $P < 0.01$).

To reveal the underlying mechanism of tumor growth inhibition by the NPs, the proliferation and apoptosis levels in the tumor sections were further analyzed by immunohistochemistry using the Ki67 and TUNEL assays. Photographs of tumor sections are illustrated in Fig. 8B. Almost no cell apoptosis was observed in groups treated with saline. The tissues of mice treated with free DOX and free OA demonstrated moderate cell apoptosis, while apoptosis most extensive in the FA-CS-g-OA@DOX group.

Quantitative analyses of the TUNEL and Ki67 data are displayed in Fig. 8C. The proliferation percentage determined by Ki67 immunohistochemistry following treatment with FA-CS-g-OA@DOX NPs ($3.8 \pm 0.6\%$) was far less than that with free DOX ($25.7 \pm 3.1\%$), free OA ($46.4 \pm 4.2\%$) and the saline control group ($90.7 \pm 8.6\%$). Moreover, the percentage of apoptotic cells measured by the TUNEL assay after treatment with FA-CS-g-OA@DOX NPs ($82.8 \pm 7.9\%$) was much higher than that with free DOX ($55.8 \pm 5.1\%$) and OA ($21.8 \pm 1.6\%$). Therefore, the NPs act to both induce apoptosis and inhibit cell proliferation in tumor tissues. All these findings demonstrate the effectiveness of the dual-drug-loaded NPs for targeted combination therapy in breast tumors [47].
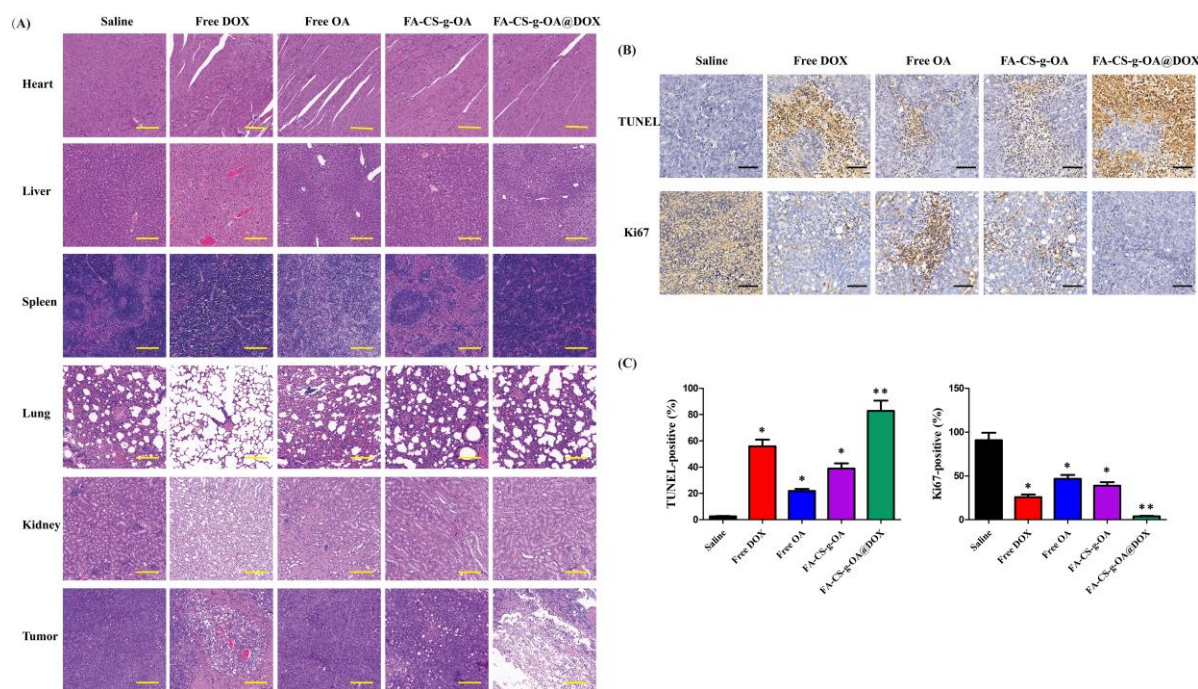
Fig. 8. Histopathology data for tumor-bearing mice. (A) Sections of heart, liver, spleen, lung, kidney and tumor stained with hematoxylin and eosin. (B) TUNEL staining and Ki67 immunohistochemistry of tumor sections. (C) Statistical analysis of the TUNEL and Ki67 positive rates ($n = 8$, results shown as mean ± S.D.; * indicates $P < 0.05$, ** indicates $P < 0.01$). Scale bars are 100 μm in the H&E assay and are 50 μm in the TUNEL and Ki67 assays.

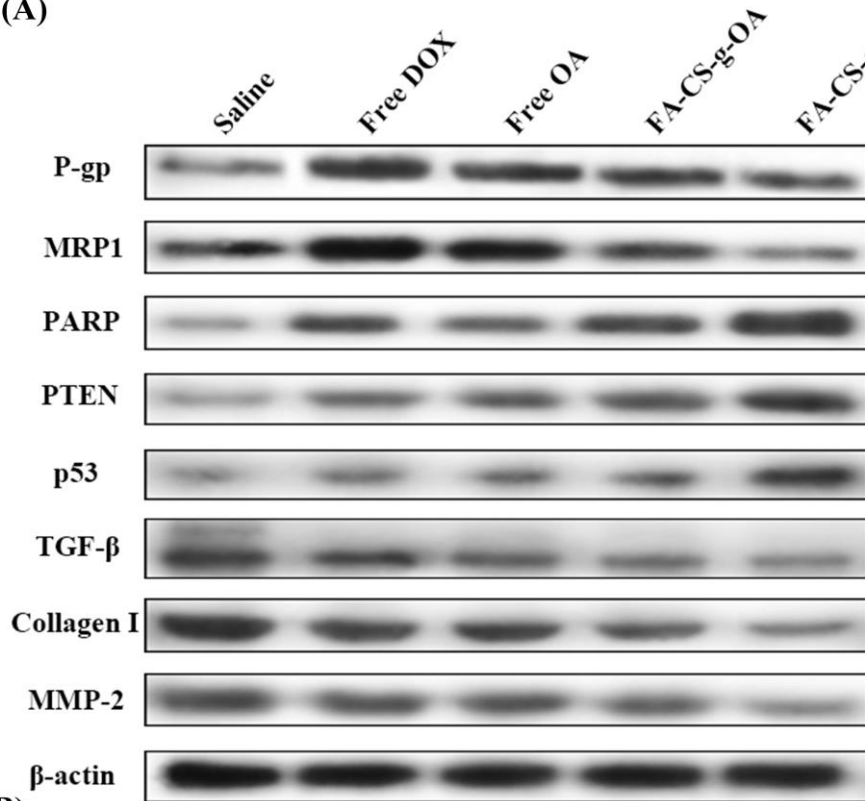## 3.9. Effects of FA-CS-g-OA@DOX NPs on protein expression

MDR is often associated with the overexpression of the drug transporters P-gp and MRP1 [48], which confer resistance to cancer cells by active excretion of a wide range of drugs from the cytosol [49]. Considerable efforts have been devoted to the development of specific molecules that can inhibit the function of P-gp and MRP1 in order to sensitize tumor cells to conventional chemotherapeutics [50], and OA is known to have such properties [27]. The expression of MRP1 and P-gp and cancer suppressive factors including PARP, PTEN and p53 were assessed by western blot. As can be seen in Fig. 9, there is a significant increase of P-gp expression in animals treated with DOX compared to those receiving saline. This indicates that DOX induced MDR and thus resulted in an increase of P-gp levels. Compared to the group treated with DOX, levels of P-gp expression are decreased by 61.4%, 36.9% and 25.3% upon treatment with FA-CS-g-OA@DOX NPs, FA-CS-g-OA and free OA, respectively. Although free OA should be potent in downregulating P-gp it has no targeting ability, and its inclusion in NPs selective for FA-over-expressing cells led to greater OA accumulation in the tumor site and greater reductions in P-gp expression. A similar trend was displayed in the expression levels of MRP1 (Fig. 9).

MDA-MB-231 cells originally expressed a high level of MRP1. When treated with FA-CS-g-OA@DOX NPs, the expression of MRP1 was almost undetectable, suggesting that the inclusion of OA in the particles is able to shut down at least some MDR mechanisms.

In order to verify the molecular mechanism of anti-tumor effects induced by FA-CS-g-OA@DOX NPs, we assessed three apoptosis-related protein expression levels (PARP, PTEN and p53) in MDA-MB-231 tumor-bearing mice. We found (Fig. 9) that when mice were treated with OA and OA-containing NPs, an increase in the expression of all three was observed. Notably, FA-CS-g-OA@DOX NPs could significantly upregulate the levels of PARP, PTEN and p53 compared with OA and the other formulations, demonstrating the enormous potential of FA-CS-g-OA@DOX NPs to induce tumoral cell apoptosis [51]. The effect of FA-CS-g-OA on the levels of PARP, PTEN and p53 was slightly greater than that of free OA, which may arise from the active targeting effects of the FA, and acidic microenvironment-triggered OA release. All these data suggest that OA could be a good choice in the treatment of MDR tumors, either as an adjuvant or as a chemotherapeutic itself [52].

With fast tumor growth, the extracellular matrix (ECM) will create growth-induced solid stress, impeding the penetration of both macromolecules and nanomedicines [53] [54]. The transforming growth factor (TGF-β) autocrine pathway plays a major role in ECM proliferation, which can also stimulate collagen I and matrix metalloproteinase (MMP) production, eventually exacerbating fibrosis in tumors. Therefore, the effects of OA on breast tumors was estimated through the change in expression of TGF-β, MMP-2 and collagen I [17] (Fig. 9). There are small reductions in TGF-β, MMP-2 and collagen I expression with free DOX and free OA. These are much more noticeable for the FA-CS-g-OA and FA-CS-g-OA@DOX NPs, which significantly inhibited the expression of TGF-β, MMP-2 and collagen I. These results illustrate that the FA-CS-g-OA@DOX NPs were able to downregulate the expression of these proteins in tumoral cells, and thus can have an anti-fibrosis effect through the TGF-β/MMP/collagen I signal pathway [5].
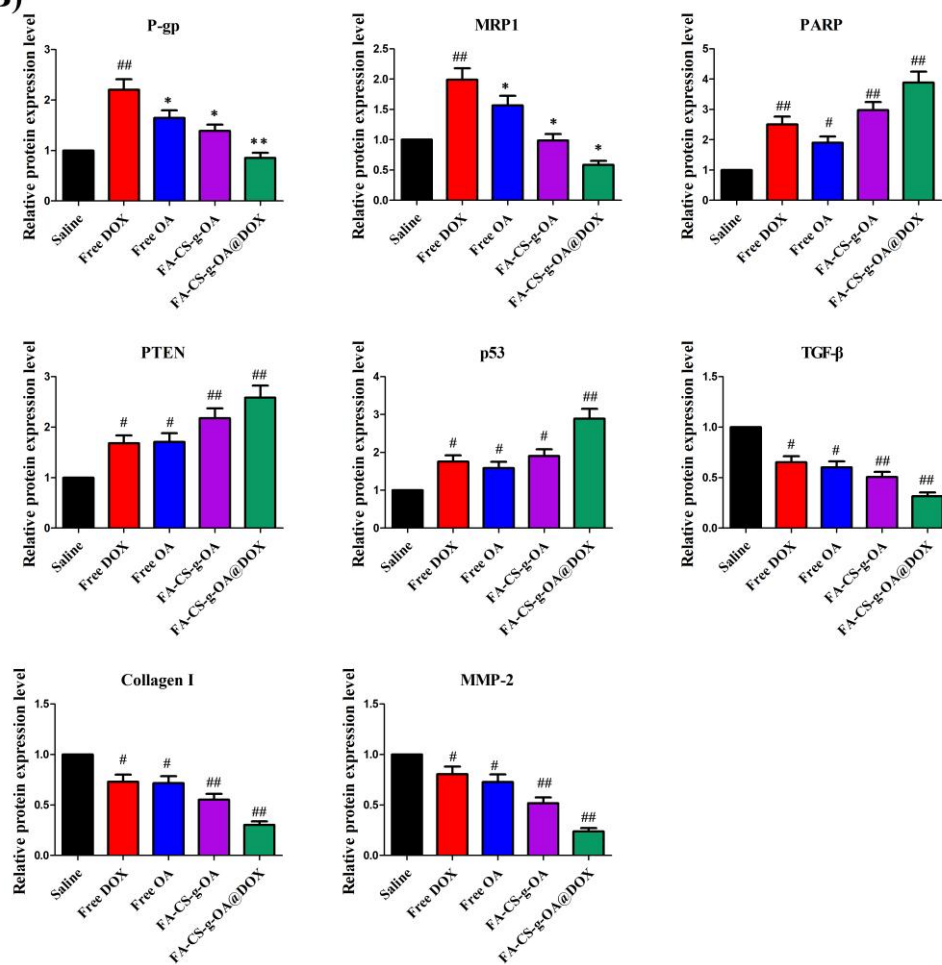
(A)

(B)

Fig. 9. The effect of treatment with saline, free DOX, free OA, FA-CS-g-OA, and FA-CS-g-OA@DOX on the protein expression profile of MDA-MB-231 breast tumors. (A) Representative photos of tumor tissues after western blot analysis. (B) Statistical analysis of protein expression levels. The blots were analyzed by densitometry and normalized to β-actin. [#]$P < 0.05$, [##]$P < 0.01$ as compared to saline group; * $P < 0.05$, ** $P < 0.01$ as compared to free DOX group. Data represent mean ± SD ($n = 6$).

3.10. Evaluation of side effects

DOX is widely associated with serious side effects, including liver and kidney damage, oxidative stress and inflammation reactions [55]. Previous work suggests that OA can have a number of biological actions, with antioxidant, anti-inflammatory, and hepatoprotective properties [56]. The serum levels of key clinical biomarkers were thus assessed to determine if the OA in the FA-CS-g-OA@DOX NPs could mitigate against these effects of DOX. An increase in the levels of biochemical markers including aspartate aminotransferase (AST), alanine aminotransferase (ALT), blood urea nitrogen (BUN), and creatinine (CRE) would be indicative of organ failure. A dramatic increase in AST, ALT, BUN, and CRE levels was observed in DOX-treated mice (Fig. 10A, B), indicating DOX-induced tissue damage. After administration of OA and OA containing NPs, however, the activity of ALT and AST is significantly reduced compared to DOX alone ($P < 0.01$) (Fig. 10A). There was no significant difference between free OA and the OA-loaded NPs ($P > 0.05$). The CRE and BUN levels induced by FA-CS-g-OA@DOX NPs are also significantly lower than those of mice treated with free DOX (Fig. 10B), and close to those in the saline group, confirming that the NPs greatly reduce the renal toxicity of free DOX.

DOX-induced hepatotoxicity involves not only hepatic injury but also the induction of oxidative stress, and thus we examined the levels of glutathione peroxidase (GSH-Px), malondialdehyde (MDA), and superoxide dismutase (SOD) in serum (Fig. 10C). MDA is a typical marker of oxidative stress and elevated concentrations in the serum are seen after DOX treatment. However, the combinational delivery of OA and DOX from the NPs significantly reduced the MDA level ($P < 0.01$). This is consistent with a previous study [57]. GSH-Px and SOD are two enzymes which protect organisms from oxidative damage. DOX treatment reduced the levels of both GSH-Px and SOD in the serum, but FA-CS-g-OA@DOX NPs reversed this because of the protective action of OA (Fig. 10C) [58].

Finally, to evaluate the effect of OA on inflammation in DOX-treated mice, serum levels of IL-1β, IL-6 and TNF-a were determined. From Fig. 10D, it is clear that DOX treated mice

exhibited high levels of serum IL-1β, IL-6 and TNF-α, but these are much reduced upon simultaneous OA administration with the FA-CS-g-OA@DOX NPs.
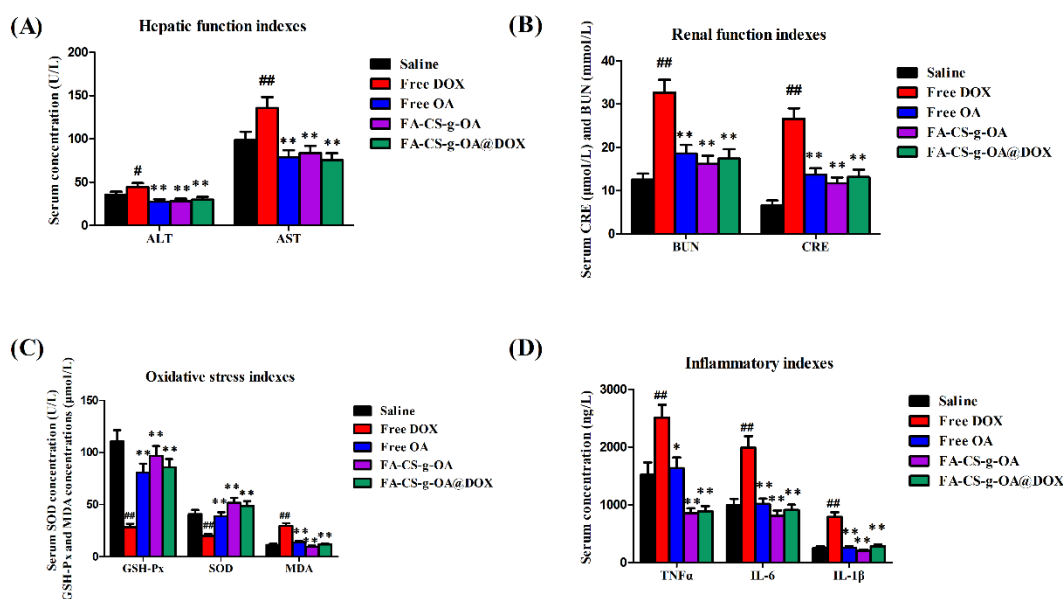

Fig. 10. The influence of the various formulations (saline, free DOX, free OA, FA-CS-g-OA, and FA-CS-g-OA@DOX) on key biomarkers for side effects. (A) Serum hepatic function indices. (B) Serum renal function indices. (C) Serum oxidative stress indices. (D) Serum inflammatory indices. [#]$P < 0.05$, [##]$P < 0.01$ as compared to the saline group; * $P < 0.05$, ** $P < 0.01$ as compared to the free DOX group. Data are given as mean ± SD ($n = 6$).

4. Conclusions

In this work, we report the synthesis, characterization and an *in vitro* and *in vivo* anti-tumor evaluation of a pH-responsive nanomedicine for the targeted co-delivery of oleanolic acid (OA) and doxorubicin (DOX). Chitosan was first functionalized with folic acid (FA) to allow active targeting to FA-receptor positive cancer cells, and the FA-CS composite further modified with OA to give FA-CS-g-OA. The latter self-assembled into nanoparticles upon addition to an aqueous medium, and DOX could be effectively trapped in the core (drug loading: 15.6 % w/w). Drug release is accelerated at the slightly acidic pHs which typify the tumor microenvironment. Enhanced cytotoxicity and cellular uptake of the FA-CS-g-OA@DOX NPs into MDA-MB-231 cells *in vitro* was noted compared with free DOX, while the NPs were less toxic than DOX to healthy HUVEC cells. *In vivo* studies demonstrated prolonged pharmacokinetics with the NPs, and reduced hemolysis. In a murine MDA-MB-231 tumor model, the FA-CS-g-OA@DOX NPs became localized in the tumor, and caused significantly greater reductions in tumor volume than

pure DOX. Systemic toxicity was reduced, and survival times increased, when using the nanoparticle formulations. The NPs caused downregulation of the P-gp and MRP-1 proteins associated with multi-drug resistance, and reduced tumor fibrosis. The presence of OA could mitigate DOX-induced tissue damage by inhibiting hepatic/renal injury, and also through anti-oxidant and anti-inflammatory activities. Taken together, our results demonstrate that the FA-CS-g-OA@DOX NPs comprise a powerful therapeutic platform for treating multi-drug resistant breast cancers.

Disclosure

The authors have no conflict of interest to declare.

Acknowledgements

References

[1] L.A. Torre, F. Bray, R.L. Siegel, J. Ferlay, J. Lortet-Tieulent, A. Jemal, Global cancer statistics, 2012, CA Cancer J Clin 65 (2015) 87-108.

[2] E. Goldman, A. Zinger, D.S. Da, Z. Yaari, A. Kajal, D. Vardioknin, M. Goldfeder, J. Schroeder, J.R. Shainsky, D. Hershkovitz, Nanoparticles target early-stage breast cancer metastasis in vivo, Nanotechnology 28 (2017) 43LT01.

[3] C. Liang, L. Xu, G. Song, Z. Liu, Emerging nanomedicine approaches fighting tumor metastasis: animal models, metastasis-targeted drug delivery, phototherapy, and immunotherapy, Chem. Soc. Rev. 45 (2016) 6250-69.

[4] M. Al-Hajj, M.S. Wicha, A. Benito-Hernandez, S.J. Morrison, M.F. Clarke, Prospective identification of tumorigenic breast cancer cells, Proc Natl Acad Sci 100 (2003) 3983-8.

[5] T. Ji, S. Li, Y. Zhang, J. Lang, Y. Ding, X. Zhao, R. Zhao, Y. Li, J. Shi, J. Hao, Y. Zhao, G. Nie, An MMP-2 Responsive Liposome Integrating Antifibrosis and Chemotherapeutic Drugs for Enhanced Drug Perfusion and Efficacy in Pancreatic Cancer, ACS Appl. Mater. interfaces 8 (2016) 3438-45.

[6] A. Arminan, M. Palomino-Schatzlein, C. Deladriere, J.J. Arroyo-Crespo, S. Vicente-Ruiz, M.J. Vicent, A. Pineda-Lucena, Metabolomics facilitates the discrimination of the specific anti-cancer effects of free- and polymer-conjugated doxorubicin in breast cancer models, Biomaterials 162 (2018) 144-53.

[7] S. Niu, D.H. Bremner, J. Wu, J. Wu, H. Wang, H. Li, Q. Qian, H. Zheng, L. Zhu, L-peptide

functionalized dual-responsive nanoparticles for controlled Paclitaxel release and enhanced apoptosis in breast cancer cells, Drug Deliv 25 (2018) 1275-88.

[8] S.Y. Qin, A.Q. Zhang, S.X. Cheng, L. Rong, X.Z. Zhang, Drug self-delivery systems for cancer therapy, Biomaterials 112 (2017) 234-47.

[9] T. Wang, J. Hou, C. Su, L. Zhao, Y. Shi, Hyaluronic acid-coated chitosan nanoparticles induce ROS-mediated tumor cell apoptosis and enhance antitumor efficiency by targeted drug delivery via CD44, J Nanobiotechnology 15 (2017) 7.

[10] M. Overchuk, G. Zheng, Overcoming obstacles in the tumor microenvironment: Recent advancements in nanoparticle delivery for cancer theranostics, Biomaterials 156 (2018) 217-37.

[11] Y. Hu, S. Mignani, J.P. Majoral, M. Shen, X. Shi, Construction of iron oxide nanoparticle-based hybrid platforms for tumor imaging and therapy, Chem. Soc. Rev. 47(2018) 1874-900.

[12] Z. Hu, J. Chen, S. Zhou, N. Yang, S. Duan, Z. Zhang, J. Su, J. He, Z. Zhang, X. Lu, Y. Zhao, Mouse IP-10 Gene Delivered by Folate-modified Chitosan Nanoparticles and Dendritic/tumor Cells Fusion Vaccine Effectively Inhibit the Growth of Hepatocellular Carcinoma in Mice, Theranostics 7 (2017) 1942-52.

[13] J.J. Wang, Z.W. Zeng, R.Z. Xiao, T. Xie, G.L. Zhou, X.R. Zhan, S.L. Wang, Recent advances of chitosan nanoparticles as drug carriers, Int J Nanomedicine 6 (2011) 765-74.

[14] J.Y. Yhee, S. Jeon, H.Y. Yoon, M.K. Shim, H. Ko, J. Min, J.H. Na, H. Chang, H. Han, J.H. Kim, M. Suh, H. Lee, J.H. Park, K. Kim, I.C. Kwon, Effects of tumor microenvironments on targeted delivery of glycol chitosan nanoparticles, J Control Release 267 (2017) 223-31.

[15] K. Jiang, T. Chi, T. Li, G. Zheng, L. Fan, Y. Liu, X. Chen, S. Chen, L. Jia, J. Shao, A smart pH-responsive nano-carrier as a drug delivery system for the targeted delivery of ursolic acid: suppresses cancer growth and metastasis by modulating P53/MMP-9/PTEN/CD44 mediated multiple signaling pathways, Nanoscale 9 (2017) 9428-39.

[16] Y. Chen, S. Feng, W. Liu, Z. Yuan, P. Yin, F. Gao, Vitamin E Succinate-Grafted-Chitosan Oligosaccharide/RGD-Conjugated TPGS Mixed Micelles Loaded with Paclitaxel for U87MG Tumor Therapy, Mol. Pharm. 14 (2017) 1190-203.

[17] M.S. Kim, J.Y. Han, S.H. Kim, D. Jeon, H.Y. Kim, S.W. Lee, M.C. Rho, K. Lee, Oleanolic acid acetate attenuates polyhexamethylene guanidine phosphate-induced pulmonary inflammation and fibrosis in mice, Resp. Physiol. Neurobi 252-253 (2018) 1-9.

[18] X. Wang, R. Liu, W. Zhang, X. Zhang, N. Liao, Z. Wang, W. Li, X. Qin, C. Hai, Oleanolic acid improves hepatic insulin resistance via antioxidant, hypolipidemic and anti-inflammatory effects, Mol. Cell. Endocrinol. 376 (2013) 70-80.

[19] Y. Xu, B. Shu, Y. Tian, G. Wang, Y. Wang, J. Wang, Y. Dong, Oleanolic acid induces osteosarcoma cell apoptosis by inhibition of Notch signaling, Mol. Carcinog. 57 (2018) 896-902.

[20] J. Hwang-Bo, M.G. Bae, J.H. Park, I.S. Chung, 3-O-Acetyloleanolic acid inhibits VEGF-A-induced lymphangiogenesis and lymph node metastasis in an oral cancer sentinel lymph node animal model, BMC Cancer 18 (2018) 714.

[21] X. Fan, P. Wang, Y. Sun, J. Jiang, H. Du, Z. Wang, Z. Duan, H. Lei, H. Li, Induction of apoptosis by an oleanolic acid derivative in SMMC-7721 human hepatocellular carcinoma cells is associated with mitochondrial dysfunction, Oncol Lett 15 (2018) 2821-8.

[22] S.A. Fisher, R.Y. Tam, A. Fokina, M.M. Mahmoodi, M.D. Distefano, M.S. Shoichet, Photo-immobilized EGF chemical gradients differentially impact breast cancer cell invasion and drug response in defined 3D hydrogels, Biomaterials 178 (2018) 751-66.

[23] L.M. Preciado, P. Rey-Suarez, I.C. Henao, J.A. Pereanez, Betulinic, oleanolic and ursolic acids inhibit the enzymatic and biological effects induced by a P-I snake venom metalloproteinase, Chem Biol Interact 279 (2018) 219-26.

[24] M. Sarfraz, A. Afzal, S.M. Raza, S. Bashir, A. Madni, M.W. Khan, X. Ma, G. Xiang, Liposomal co-delivered oleanolic acid attenuates doxorubicin induced multi-organ toxicity in hepatocellular carcinoma, Oncotarget 8 (2017) 47136-53.

[25] H. Meng, M. Liong, T. Xia, Z. Li, Z. Ji, J.I. Zink, A.E. Nel, Engineered design of mesoporous silica nanoparticles to deliver doxorubicin and P-glycoprotein siRNA to overcome drug resistance in a cancer cell line, ACS nano 4 (2010) 4539-50.

[26] K. Nooter, H. Herweijer, Multidrug resistance (mdr) genes in human cancer, Br. J. Cancer 63 (1991) 663-9.

[27] F. Braga, D. Ayres-Saraiva, C.R. Gattass, M.A. Capella, Oleanolic acid inhibits the activity of the multidrug resistance protein ABCC1 (MRP1) but not of the ABCB1 (P-glycoprotein): possible use in cancer chemotherapy, Cancer Lett. 248 (2007) 147-52.

[28] J.Y. Lee, U. Termsarasab, M.Y. Lee, D.H. Kim, S.Y. Lee, J.S. Kim, H.J. Cho, D.D. Kim, Chemosensitizing indomethacin-conjugated chitosan oligosaccharide nanoparticles for tumor-targeted drug delivery, Acta Biomater. 57 (2017) 262-73.

[29] A. Wan, Y. Sun, H. Li, Characterization of folate-graft-chitosan as a scaffold for nitric oxide release, Int J Biol Macromol 43 (2008) 415-21.

[30] Y. Zhong, M. Dimde, D. Stöbener, F. Meng, C. Deng, Z. Zhong, R. Haag, Micelles with Sheddable Dendritic Polyglycerol Sulfate Shells Show Extraordinary Tumor Targetability and Chemotherapy In Vivo, ACS Appl. Mater. Interfaces 8 (2016) 27530-8.

[31] X. Song, Z. Wan, T. Chen, Y. Fu, K. Jiang, X. Yi, H. Ke, J. Dong, L. Yang, L. Li, X. Sun, T. Gong, Z. Zhang, Development of a multi-target peptide for potentiating chemotherapy by modulating tumor microenvironment, Biomaterials 108 (2016) 44-56.

[32] H. Wang, P. Agarwal, S. Zhao, J. Yu, X. Lu, X. He, Combined cancer therapy with hyaluronan-decorated fullerene-silica multifunctional nanoparticles to target cancer stem-like cells, Biomaterials 97 (2016) 62-73.

[33] J. Gao, C. Xie, M. Zhang, X. Wei, Z. Yan, Y. Ren, M. Ying, W. Lu, RGD-modified lipid disks as drug carriers for tumor targeted drug delivery, Nanoscale 8(2016) 7209-16.

[34] J. Wu, D.H. Bremner, S. Niu, H. Wu, J. Wu, H. Wang, H. Li, L.-M. Zhu, Functionalized MoS 2 nanosheet-capped periodic mesoporous organosilicas as a multifunctional platform for synergistic targeted chemo-photothermal therapy, Chem. Eng. J. 342 (2018) 90-102.

[35] H. Zhou, W. Yu, X. Guo, X. Liu, N. Li, Y. Zhang, X. Ma, Synthesis and characterization of amphiphilic glycidol-chitosan-deoxycholic acid nanoparticles as a drug carrier for doxorubicin, Biomacromolecules 11(2010) 3480-6.

[36] L. Zhang, J. Wang, C. Ni, Y. Zhang, G. Shi, Preparation of polyelectrolyte complex nanoparticles of chitosan and poly(2-acry1amido-2-methylpropanesulfonic acid) for doxorubicin release, Mater Sci Eng C Mater Biol Appl 58 (2016) 724-9.

[37] Y. Yu, C.K. Chen, W.C. Law, E. Weinheimer, S. Sengupta, P.N. Prasad, C. Cheng, Polylactide-graft-doxorubicin nanoparticles with precisely controlled drug loading for pH-triggered drug delivery, Biomacromolecules 15(2014) 524-32.

[38] P.T. Wong, S.K. Choi, Mechanisms of drug release in nanotherapeutic delivery systems, Chem. Rev. 115 (2015) 3388-432.

[39] J. Yang, X. Liu, K. Bhalla, C.N. Kim, A.M. Ibrado, J. Cai, D.P. Jones, X. Wang, Prevention of Apoptosis by Bcl-2: Release of Cytochrome c from Mitochondria Blocked, Science 275 (1997) 1129.

[40] Z. Hou, C. Zhan, Q. Jiang, Q. Hu, L. Li, D. Chang, X. Yang, Y. Wang, Y. Li, S. Ye, L. Xie, Y. Yi, Q. Zhang, Both FA- and mPEG-conjugated chitosan nanoparticles for targeted cellular uptake and enhanced tumor tissue distribution, Nanoscale Res Lett 6 (2011) 563.

[41] Y. Zhang, X. Tan, T. Ren, C. Jia, Z. Yang, H. Sun, Folate-modified carboxymethyl-chitosan/polyethylenimine/bovine serum albumin based complexes for tumor site-specific drug delivery, Carbohydr. Polym. 198 (2018) 76-85.

[42] J. Liu, Z. Luo, J. Zhang, T. Luo, J. Zhou, X. Zhao, K. Cai, Hollow mesoporous silica nanoparticles facilitated drug delivery via cascade pH stimuli in tumor microenvironment for tumor therapy, Biomaterials 83 (2016) 51-65.

[43] U. Luesakul, S. Puthong, N. Neamati, N. Muangsin, pH-responsive selenium nanoparticles stabilized by folate-chitosan delivering doxorubicin for overcoming drug-resistant cancer cells, Carbohydr. Polym. 181 (2018) 841-50.

[44] L. Fan, F. Li, H. Zhang, Y. Wang, C. Cheng, X. Li, C.H. Gu, Q. Yang, H. Wu, S. Zhang, Co-delivery of PDTC and doxorubicin by multifunctional micellar nanoparticles to achieve active targeted drug delivery and overcome multidrug resistance, Biomaterials 31(2010) 5634-42.

[45] S. Hua, J. Yu, J. Shang, H. Zhang, J. Du, Y. Zhang, F. Chen, Y. Zhou, F. Liu, Effective tumor-targeted delivery of etoposide using chitosan nanoparticles conjugated with folic acid and sulfobetaine methacrylate, RSC Adv. 6 (2016) 91192-200.

[46] L. Lin, Y. Fan, F. Gao, L. Jin, D. Li, W. Sun, F. Li, P. Qin, Q. Shi, X. Shi, L. Du, UTMD-Promoted Co-Delivery of Gemcitabine and miR-21 Inhibitor by Dendrimer-Entrapped Gold Nanoparticles for Pancreatic Cancer Therapy, Theranostics 8 (2018) 1923-39.

[47] Y. Fan, Q. Wang, G. Lin, Y. Shi, Z. Gu, T. Ding, Combination of using prodrug-modified cationic liposome nanocomplexes and a potentiating strategy via targeted co-delivery of gemcitabine and docetaxel for CD44-overexpressed triple negative breast cancer therapy, Acta Biomater. 62 (2017) 257-72.

[48] H. Wang, X.H. Jia, J.R. Chen, Y.J. Yi, J.Y. Wang, Y.J. Li, S.Y. Xie, HOXB4 knockdown reverses multidrug resistance of human myelogenous leukemia K562/ADM cells by downregulating P-gp, MRP1 and BCRP expression via PI3K/Akt signaling pathway, Int. J. Oncol. 49 (2016) 2529-37.

[49] U.M. Alfred H. Schinkel, Els Wagenaar, Carla A. A. M. Mol, Liesbeth van Deemter, Jaap J. M. Smit, Martin A. van der Valk, Arie C. Voordouw, Hergen Spits, Olaf van Tellingen, J. Mark J. M. Zijlmans, Willem E. Fibbe, Piet Borst, Normal Viability and Altered Pharmacokinetics in Mice Lacking mdr1-Type (Drug-Transporting) P-Glycoproteins, Proc Natl Acad Sci 94 (1997) 4028-33.

[50] X.B. Xiong, A. Lavasanifar, Traceable multifunctional micellar nanocarriers for cancer-targeted co-delivery of MDR-1 siRNA and doxorubicin, ACS nano 5 (2011) 5202-13.

[51] D. Guo, S. Xu, Y. Huang, H. Jiang, W. Yasen, N. Wang, Y. Su, J. Qian, J. Li, C. Zhang, X. Zhu, Platinum(IV) complex-based two-in-one polyprodrug for a combinatorial chemo-photodynamic therapy, Biomaterials 177 (2018) 67-77.

[52] Y.K. Lee, J. Choi, W. Wang, S. Lee, T.H. Nam, W.S. Choi, C.J. Kim, J.K. Lee, S.H. Kim, S.S. Kang, Nullifying tumor efflux by prolonged endolysosome vesicles: development of low dose anticancer-carbon nanotube drug, ACS nano 7 (2013) 8484-97.

[53] T. Ji, Y. Ding, Y. Zhao, J. Wang, H. Qin, X. Liu, J. Lang, R. Zhao, Y. Zhang, J. Shi, N. Tao, Z.

Qin, G. Nie, Peptide assembly integration of fibroblast-targeting and cell-penetration features for enhanced antitumor drug delivery, Adv. Mater. 27 (2015) 1865-73.

[54] T. Ji, Y. Zhao, Y. Ding, J. Wang, R. Zhao, J. Lang, H. Qin, X. Liu, J. Shi, N. Tao, Z. Qin, G. Nie, Y. Zhao, Transformable Peptide Nanocarriers for Expeditious Drug Release and Effective Cancer Therapy via Cancer-Associated Fibroblast Activation, Angew. Chem. Int. Ed. 55 (2016) 1050-5.

[55] H. Hu, Y. Li, Q. Zhou, Y. Ao, C. Yu, Y. Wan, H. Xu, Z. Li, X. Yang, Redox-Sensitive Hydroxyethyl Starch-Doxorubicin Conjugate for Tumor Targeted Drug Delivery, ACS Appl. Mater. Interfaces 8 (2016) 30833-44.

[56] L. Luo, Y. Bian, Y. Liu, X. Zhang, M. Wang, S. Xing, L. Li, D. Gao, Combined Near Infrared Photothermal Therapy and Chemotherapy Using Gold Nanoshells Coated Liposomes to Enhance Antitumor Effect, Small 12(2016) 4103-12.

[57] D. Wang, B. Liu, Y. Ma, C. Wu, Q. Mou, H. Deng, R. Wang, D. Yan, C. Zhang, X. Zhu, A Molecular Recognition Approach To Synthesize Nucleoside Analogue Based Multifunctional Nanoparticles for Targeted Cancer Therapy, J. Am. Chem. Soc. 139(2017) 14021-4.

[58] R. Tao, M. Gao, F. Liu, X. Guo, A. Fan, D. Ding, D. Kong, Z. Wang, Y. Zhao, Alleviating the Liver Toxicity of Chemotherapy via pH-Responsive Hepatoprotective Prodrug Micelles, ACS Appl. Mater. interfaces 10(2018) 21836-46.

Graphical Abstract
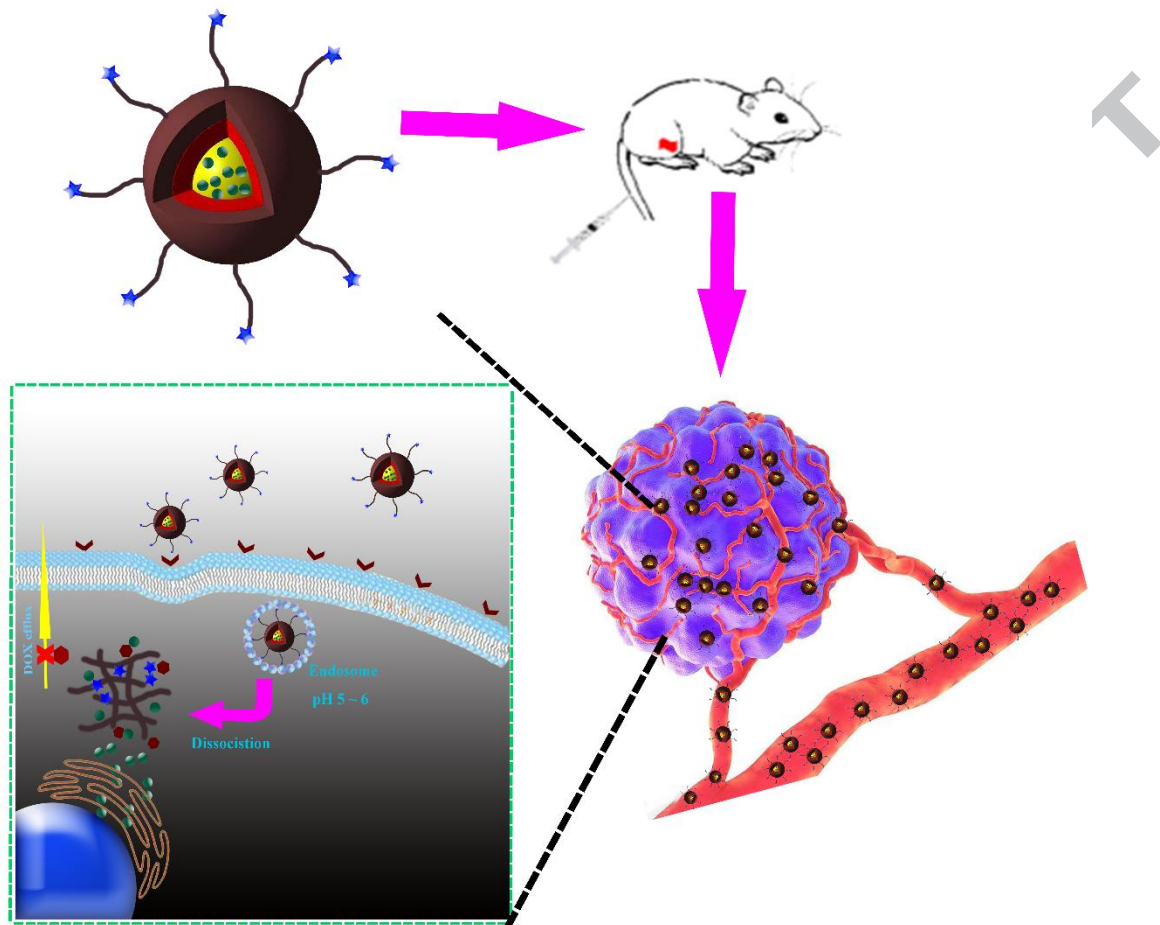
H I G H L I G H T S

- A novel doxorubicin formulation was fabricated to treat multi-drug resistant tumors.

- The oleanolic acid modified composite can ameliorate the off-target side effects.

- The nanocomposite can increase the drug penetration via anti-fibrosis pathway.

- The nanocomposite can target tumor cells, and provides synergistic cancer therapy.